SIMULATIONS FOR A 2.6 M TALL DUAL-PHASE XENON TIME PROJECTION CHAMBER

A THESIS

submitted by

RACHANA S YAJUR

in partial fulfilment of the requirements
for the award of the degree of

BACHELOR OF SCIENCE & MASTER OF SCIENCE

DEPARTMENT OF PHYSICS
INDIAN INSTITUTE OF TECHNOLOGY MADRAS.

June, 2020

THESIS CERTIFICATE

This is to certify that the thesis titled **SIMULATIONS FOR A 2.6 M TALL DUAL-PHASE XENON TIME PROJECTION CHAMBER**, submitted by **Rachana S Yajur**, to the Indian Institute of Technology, Madras, for the award of the degree of **BS&MS** in Physics, is a bona fide record of the research work done by her under our supervision. The contents of this thesis, in full or in parts, have not been submitted to any other Institute or University for the award of any degree or diploma.

Prof. Laura Baudis
Research Guide
Professor
Physik Institut
University of Zürich

Place:
Date:

Prof. Jim Libby
Co-Guide
Professor
Department of Physics
IIT Madras

Place:
Date:

Acknowledgements

I am extremely grateful to Prof. Laura Baudis for providing me the wonderful opportunity to work with her group at the University of Zürich. The four months time spent in Zürich was a great learning experience for me.

I would like to thank Dr. Alessandro Manfredini for patiently guiding me through the thesis work and the wonderful discussions on the workings of the demonstrator. I am extremely grateful to Yanina Biondi for her unwavering help with the simulations and especially for her time and constant guidance with background simulations. I thank Dr. Patricia Sanchez for her guidance with simulations and her constant support throughout the thesis work. I am thankful to Dr. Michelle Galloway for her helpful comments and discussions. I thank Dr. Neil Mcphadden and everyone mentioned above for their detailed reviewing of this thesis. I am thankful to Kevin Theime and Frederic Girard for ideating and helping me perform the experiment to test SiPM field of view. I would also like to thank Alexander Bismark for helping me setup the codes for light collection efficiency simulations in the initial stages. I would like to thank all the members of the astroparticle group for their hospitality during my stay in Zürich.

I would like to thank Prof. Jim Libby for being the co-guide, for his comments on the thesis and the inspiring courses in particle physics.

Finally, I would like to thank my dear friends and family for their support.

Abstract

Astrophysical and cosmological observations lead to the deduction that almost 30% of the energy density in the universe is comprised of an unknown form of matter, or dark matter as it is widely termed to be. The attempts to directly observe dark matter particles have lead to many developments in detector technologies used in experimental particle physics. One of the well established techniques for direct detection of dark matter particles involves the usage of noble liquids.

A future observatory, DARWIN, will use a multi-ton liquid xenon time projection chamber (TPC) to detect dark matter and neutrinos, among other rare interactions. As part of the DARWIN R&D programme, a 2.6 m tall dual-phase xenon TPC demonstrator is under construction in the Physics Department of the University of Zürich. The design optimization of photosensor placements and calibration sources for the 2.6 m tall demonstrator are determined by simulations performed as a part of this thesis work.

The main goal of this thesis has been to perform light collection efficiency simulations to better understand the detection efficiency of xenon scintillation light for different configurations of the photosensors placed in the detector. A simple experiment testing a single photosensor was carried out to validate a part of the light collection efficiency simulations. In addition, in order to characterize the charge and light detection capabilities of the demonstrator TPC, a detailed study of the radiogenic background due to the presence of radioisotopes in the materials surrounding the detector and in the laboratory walls was performed.

This thesis is organized as follows: An introduction to dark matter searches is described in chapter 1. Chapter 2 explains the motivation for the DARWIN experiment and its demonstrator and provides an overview of the parts involved in the detector design. Chapter 3 details the light collection efficiency simulation procedures and its results. The details and results of the experiment testing a photosensor are described in chapter 4. Background simulations are explored in chapter 5. This chapter finally connects the background simulations to the light collection efficiency simulations and provides a conclusion regarding the photosensor placements in the TPC. Chapter 6 summarises the main findings of the thesis.

Contents

Glossary

TPC	Time Projection Chamber
PMT	Photo Multiplier Tube
APD	Avalanche Photo Diode
MPPC	Multi Pixel Photon Counter
FWHM	Full Width Half Maximum
ADC	Analog to Digital Converter
MOND	MOdified Newtonian Dynamics
CMB	Cosmic Microwave Background
WIMP	Weakly Interacting Massive Particles
LHC	Large Hadron Collider
CERN	European Organization for Nuclear Research
DARWIN	DARk matter WImp search with liquid xenoN
VUV	Vacuum Ultra Violet
PTFE	Poly Tetra Fluoro Ethylene
DAQ	Data AQuisition
OFHC	Oxygen-Free High Thermal Conductivity
ER	Electronic Recoil
NR	Nuclear Recoil
LCE	Light Collection Efficiency
MC	Monte Carlo
FSR	Field Shaping Rings

1. Dark Matter Searches

The search for dark matter attempts to solve one of the most important problems in physics today. Significant evidence from astrophysical and cosmological observations confirms the presence of dark matter in our universe and in particular also in the Milky Way. Physicists have been speculating about the nature of dark matter through theoretical models and experimental searches for almost a century now. While there are multiple proposals for suitable dark matter candidates, there has been no confirmed experimental detection of a dark matter particle so far.

In this chapter, observational evidence for the existence of dark matter is discussed in section 1.1. The properties and suitable candidates for dark matter are discussed in section 1.2. Section 1.3 lists the broad classification of experiments and the current developments in dark matter detection techniques. A review of the basic principles involved in the working of noble liquid detectors is given in section 1.4.

1.1. Observational Evidence for Dark Matter

Anomalous motion of galaxies in Coma cluster

The Swiss astronomer Fritz Zwicky, examining the Coma galaxy cluster in 1933, discovered for the first time a gravitational anomaly using the virial theorem [1, 2]:

$$\frac{M_{\text{tot}} v^2}{2} = \frac{G M_{\text{tot}}^2}{4 R_{\text{tot}}}, \tag{1.1}$$

where M_{tot} is the total mass of the system, v is the dispersion velocity, R_{tot} is the radius of the cluster and G is the Newton's gravitational constant. Using this equation, Zwicky was able to measure the mass of the cluster knowing the observed dispersion velocities. That gravitational mass value was around 400 times greater than that expected from their luminosity. Hence he invoked the existence of dark matter to explain this excess of mass, which he termed dunkle (kalt) Materie.

Galaxy rotation curves

Further evidence,this time from rotation of disk galaxies were first observed by Vera Rubin [3]. Her observations showed that the rotation curves veered off from explanations provided by Newtonian dynamics.

The motivation for dark matter from galaxy rotation curves can be shown by a simple example. According to Newtonian mechanics, the rotation velocity $v(r)$ of a star/gas cloud at a distance r from the centre of the galaxy is given by the expression:

$$v(r) = \sqrt{\frac{GM(r)}{r}} \tag{1.2}$$

Where $M(r)$ is the mass enclosed within r.

This equation implies that the rotation velocity drops off when increasing the distance from the centre of the galaxy. Observations of the rotation velocities of the stars and gas shows an almost flat behavior towards the outskirts of the galaxy instead of the expected $r^{-1/2}$ dependence, as shown in figure 1.1.

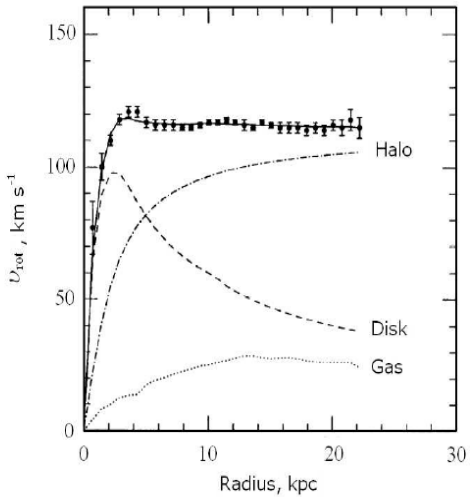

Figure 1.1.: *The rotation velocity curve of the spiral galaxy NGC6503 as a function of distance from the galactic centre (taken from [4]). In order to fit the disk and the gas contribution to the velocity function with the observed data, a dark matter halo mass function was invoked.*

A solution to this discrepancy can be established by including the presence of an additional non-luminous mass in the form of a dark matter halo which envelopes the galaxy (see figure 1.1). Alternatives to the dark matter halo in the galaxy were also proposed, such as modified Newtonian dynamics (MOND) [5].

Cosmic Microwave Background

The absolute abundance of dark matter particles in the universe can be measured from the temperature fluctuations in the cosmic microwave background (CMB), which was discovered in 1965 by Penzias and Wilson[6]. Around 380 000 years after the Big Bang, the universe became cold enough to form neutral atoms and the photons decoupled from the baryon-photon plasma. The CMB is, therefore, the relic of the last scattering before the plasma, this epoch is referred to as 'recombination'. The CMB is measured by satellites such as COBE [7], WMAP [8] and Planck[9]. Figure 1.2 shows the temperature fluctuations in the CMB spectrum as measured jointly by Planck, WMAP and 408 MHz observations. The study of the temperature power spectrum of the CMB, i.e., plotting the amount of fluctuations in the CMB temperature spectrum at different angular scales on the sky, provides information about the curvature of the universe and the total baryonic matter content. One can equate the mass energy relationships and calculate the amount of dark matter in the universe from the power spectrum [10]. The CMB and other observations in the cosmological scale also attempts to rule out the proposed theory of MOND [11].

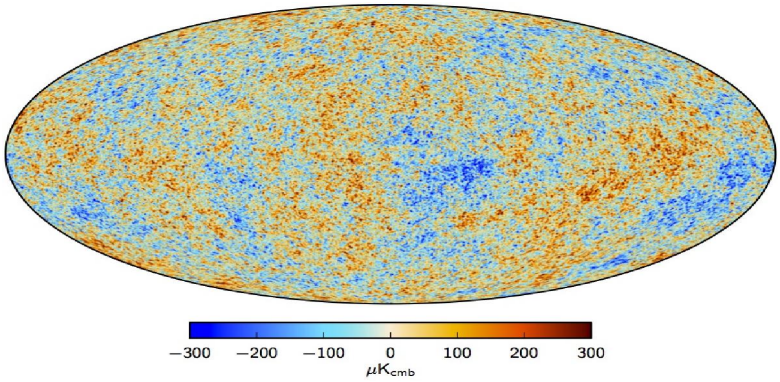

Figure 1.2.: *Sky map of temperature fluctuations in the measured cosmic microwave background derived from the joint analysis of Planck, WMAP and 408 MHz observations. Figure taken from [9].*

Gravitational Lensing

According to Einstein's general theory of relativity, mass concentrations distort space around them. When a huge amount of matter, like a cluster of galaxies, distorts space it forms something called a gravitational lens. This lens can deflect the light trajectories between an observer and distant galaxies that are behind it but in the same line of sight, producing a distorted image. The effect is called gravitational lensing. Images from the Hubble space telescope are a rich resource to observe this phenomena [12]. These images also act as a probe of the total matter distribution in a galaxy cluster, since they account for both visible and dark matter. The results indicate that most of the matter in a galaxy cluster is not in the visible galaxies or the hot gas around them. Hubble's images of

gravitational lensing have been used to create maps of dark matter in galaxy clusters, one example of which can be seen in figure 1.3.

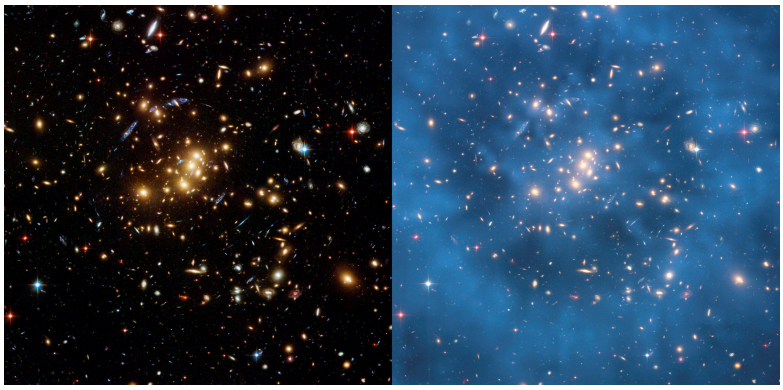

Figure 1.3.: *Left: Hubble Space Telescope image of the galaxy cluster Cl 0024+17. The view of the galaxy structures are distorted as a result of lensing. Right: The same image overlaid with a map of the cluster's mass distribution. The ring-like structure evident in the map is one of the strongest pieces of evidence to date for the existence of dark matter. Figure taken from [13].*

Galaxy Cluster Collisions

Another hint for the existence of dark matter stems from the observation of galaxy cluster collisions like that of the Bullet cluster seen in figure 1.4. During the collision of two galaxy clusters, the gas and the baryonic matter heat up and as a result form a plasma. This slows down the motion of the baryonic matter in the clusters during collision. On the other hand, the dark matter is unaffected by the heating up of the baryons and moves with a much faster velocity resulting in an accumulation towards the edge of the merged cluster.

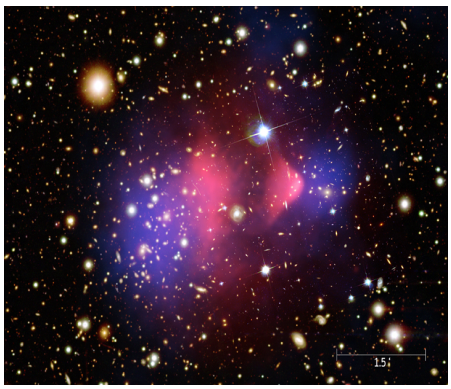

Figure 1.4.: *Superposition of X-ray image taken by the Chandra telescope of the Bullet cluster (pink) over a visible light image taken by Hubble and Magellan space telescopes, with a matter distribution calculated from gravitational lensing (blue). Figure taken from [14].*

1.2. Properties of Dark Matter

Based on the observational evidence discussed above, it can be inferred that dark matter is a new, non-baryonic form of matter. To allow for the isotropic halos in galaxies to be in a steady state, the dark matter particles have to be non-relativistic or 'cold'. This can be inferred by using the Boltzmann equation and Jeans' theorem [15]. Dark matter interacts via the gravitational force but does not seem to show electromagnetic interactions within current experimental precision. Further, cosmological evidence suggests that dark matter must be a particle beyond the standard model [16].

1.2.1. Dark Matter Candidates

With the growing evidence against alternative theories of dark matter particles like massive compact halo objects - MACHOs [17] and MOND theory, dark matter is most plausibly composed of particles that are beyond the standard model. Some candidates for dark matter particles are axions [18], WIMPzillas (superheavy dark matter) [19], sterile neutrinos [20] and the Weakly Interacting Massive Particles (WIMPs). WIMP is one of the best motivated candidates for dark matter and the focus of this thesis is on detector development for WIMP detection.

1.3. Experiments searching for dark matter

In order to establish an experimental method to detect dark matter particles, we shall proceed by making a couple of assumptions.

Assumption 1: Dark matter consists of particles (beyond the Standard Model), which at some rate interact with Standard Model particles as well as among themselves. Let the dark matter particles be denoted by χ and Standard Model particles by S.

Assumption 2: During some epoch in the universe, χ was in equilibrium with S. And hence the following equilibrium reactions took place among them:

$$\chi + \chi \rightleftharpoons S + S \tag{1.3}$$
$$\chi + S \rightleftharpoons \chi + S \tag{1.4}$$
$$S + S \rightleftharpoons \chi + \chi \tag{1.5}$$

These are the only possibilities, as $\chi+\chi \rightleftharpoons \chi+\chi$ cannot be observed and $S+S \rightleftharpoons S+S$ give us no information about dark matter. Based on these equilibrium reactions, different kinds of experiments can be developed. An overview of these experiments is described in the next section.

Following the equations presented above, the experimental detection procedure

for dark matter is broadly classified into three types: indirect, direct and collider experiments.

1.3.1. Indirect detection

This type of detection exploits the dark matter self-interaction channel as given in equation(1.3). Earth bound detectors and satellites search for annihilation products from astrophysical sources. Fermi [21], MAGIC [22], HESS [23] and CTA look for photons, IceCube [24] and ANTARES [25] search for neutrinos and PAMELA and AMS [26] can detect anti-fermions. No conclusive evidence for WIMPs or any other form of dark matter has been observed in these experiments so far.

1.3.2. Collider experiments

The Large Hadron Collider (LHC) [27] at CERN aims to produce WIMPs by the collision of two standard model particles as in equation(1.5). A signal of dark matter can be detected by a discrepancy in the energy and momenta before the collision and the total energy and momenta of the produced and detected Standard Model particles.

1.3.3. Direct detection

Direct detection experiments are earth bound and exploit the nuclear recoils produced by a WIMP-nucleus scattering as in equation(1.4). WIMP interactions with nuclei could produce a signal in the form of heat, charge or light. An experiment can measure one or two of these signals to determine the energy deposited in the detector. DAMA/LIBRA [28] and SABRE [29] experiments use solid scintillation detectors to search for an annual modulation of the WIMP rate. CRESST [30], SuperCDMS [31] and EDELWEISS [32] are based on bolometric techniques. DAMIC [33] uses charge-coupled devices (CCDs) and looks for signals in the form of charge deposition. PICO [34] uses a bubble chamber. The XMASS [35] and DEAP-3600 [36] experiments operated a single-phase detector filled with xenon and argon, respectively, which uses light to measure the signal. DarkSide [37] and ArDM [38] experiments use argon-based dual-phase time projection chamber. XENON1T [39], LZ [40] and PandaX [41], utilize xenon-based dual-phase time projection chambers (TPCs). Dual-phase TPCs look for light and charge signals. The DARWIN [42] experiment is a proposed next-generation liquid xenon TPC and will be discussed further in chapter 2

A general description of the workings of noble liquid detectors used for direct detection experiments is provided in the next section.

1.4. Dual Phase Time Projection Chamber

The noble gases neon (Ne), argon (Ar) and xenon (Xe) in liquid phase can be used as a target material for WIMP searches [43]. The three elements are excellent scintillators with very high light yields, and liquid xenon (LXe) and liquid argon (LAr) are very good ionizers as well, allowing for a direct measurement of the ionization signal induced by particle interactions. This thesis focuses on liquid xenon detectors. Properties of liquid xenon as a target material are described in the following sections.

1.4.1. Properties of Liquid Xenon

Xenon is a preferred target material in rare event searches, due to the absence of any long lived radioisotopes, besides the double-beta emitter ^{136}Xe with a half life of 2.165×10^{21} years. LXe offers excellent sensitivity to spin-dependent WIMP-nucleon cross sections due to the presence of non-zero spin isotopes such as ^{129}Xe and ^{131}Xe [44]. Some of the physical properties of liquid xenon that are exploited in detectors are listed below:

- **Atomic number and density**: LXe has a high atomic number (Z = 54) and a high density ($\sim$ 3 gm/cm^3). This makes it very efficient to stop penetrating radiation [45]. The single large homogeneous active volume of LXe provides high stopping power (self-shielding) as opposed to other scintillating media such as liquid argon.
- **Triple point**: The triple point of xenon is at 161.4 K and it can remain in the liquid state until 200 K. This is higher than the temperature of liquid nitrogen, which is commercially available and can be used in the cooling process for xenon.
- **Electronic structure**: LXe has an electronic band structure. The band gap is large enough to behave as an insulator [46]. As a result of this band structure, LXe can form excitons and excimers which are the major mediators in the scintillation process.
- **Scintillation light**: When LXe scintillates as a result of interaction with incoming particles, the light emitted will be in the vacuum ultraviolet (VUV) region. Its wavelength is peaked at 178 nm (7 eV) with a width of 13 nm.
- **Refractive index**: The refractive index of LXe at 170 K for VUV light wavelength is 1.69 ± 0.02.
- **Light attenuation length**: While LXe is transparent to VUV light, it attenuates the photon signals due to Rayleigh scattering and absorption by impurities. The attenuation length for VUV light is measured to be > 100 cm [47].

1.4.2. Liquid xenon as a scintillator

The energy transfer of a particle interaction within the LXe medium is split between ionisation, excitation and heat. The major intermediate in the scintillation of LXe is the production of excited molecules, excimers. An excimer (Xe_2^*) will be produced by the following process with 'd' being the interacting particle:

$$\mathrm{d} + \mathrm{Xe} \rightarrow \mathrm{Xe}^+ + e \tag{1.6}$$
$$\mathrm{Xe}^+ + \mathrm{Xe} \rightarrow \mathrm{Xe}_2^+ \tag{1.7}$$
$$\mathrm{Xe}_2^+ + e^- \rightarrow \mathrm{Xe}^{**} + \mathrm{Xe} \tag{1.8}$$
$$\mathrm{Xe}^{**} \rightarrow \mathrm{Xe}^* + \mathrm{heat} \tag{1.9}$$
$$\mathrm{Xe}^* + \mathrm{Xe} \rightarrow \mathrm{Xe}_2^* \tag{1.10}$$

The excimer can also be produced by a more direct process:

$$\mathrm{d} + \mathrm{Xe} \rightarrow \mathrm{Xe}^* \tag{1.11}$$
$$\mathrm{Xe}^* + \mathrm{Xe} \rightarrow \mathrm{Xe}_2^* \tag{1.12}$$

The excimers decay within a few nanoseconds from the singlet or triplet spin state further to the ground state by the emission of a VUV photon.

$$\mathrm{Xe}_2^* \rightarrow 2\mathrm{Xe} + \gamma \tag{1.13}$$

The xenon atoms do not absorb the scintillation light and hence are transparent to the emitted VUV photons produced by the de-excitation of the excimers. Xenon is considered a fast scintillator.

1.4.3. Working principle of a dual-phase xenon TPC

A particle interaction inside the active liquid xenon creates both scintillation photons and ionisation electrons. The xenon-based dual-phase TPC measures the prompt scintillation signal and the ionisation signal of an energy deposition in liquid xenon. In figure 1.5 the working principle is shown. The TPC consists of an active liquid xenon target and a gaseous xenon (GXe) part on top. Photosensors are placed on top and bottom of the active xenon volume. The prompt scintillation photons (S1) are detected by both arrays of photosensors below and above the target. A homogeneous drift field applied across the target ($\vec{E}_{\mathrm{drift}}$) drifts the electrons from the interaction site to the LXe/GXe boundary. The electrons are extracted into the gas phase by a strong extraction field ($\vec{E}_{\mathrm{extraction}}$) which ensures a near 100 % extraction efficiency. The electrons are accelerated to the high field region in GXe and they produce an electro-luminescence signal (S2) as a result

of cascading effect. This S2 signal is proportional to the number of extracted electrons.

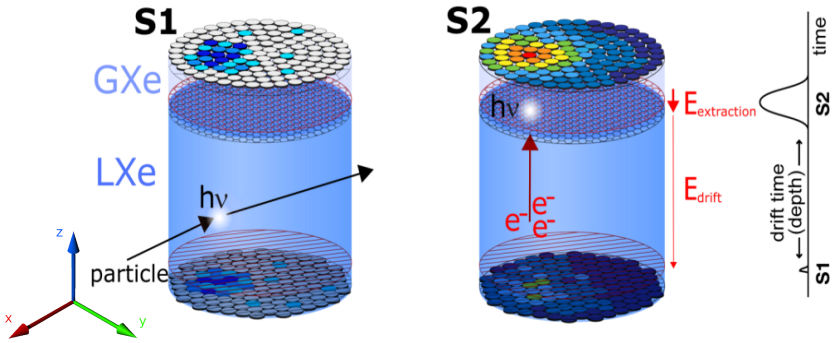

Figure 1.5.: *Working principle of a xenon-based dual-phase TPC. A particle interaction inside the active liquid xenon creates both scintillation photons and ionisation electrons. The scintillation photons (labelled hν) are detected by two photosensor arrays below and above the target. Figure adapted from that in Ref.[48]*

.

The time delay between the S1 and S2 signals can be used to determine the z coordinate of the interaction site. The S2 signal is strongly localized in the $x-y$ plane, and therefore, the collection pattern on the top photosensor array can be used to reconstruct the x and y coordinates of the interaction. The ratio of the two signals (S2/S1) is used for background event discrimination and particle identification.

2. The DARWIN experiment and its 2.6 m long demonstrator

2.1. DARWIN

DARk matter WImp search with liquid xenoN (DARWIN) will be an observatory for the direct detection of WIMPs with masses above 5 GeV/c^2 [42]. It will use a multi-ton (50 t total with 40 t active) LXe TPC at its core. The experiment's primary goal will be to explore the experimentally accessible parameter space for WIMPs in a wide mass-range, until neutrino interactions with the target become an irreducible background. Besides WIMPs, it also aims to detect solar *pp*-neutrinos with high statistics, observe coherent neutrino-nucleus interactions and search for solar axions, axion like particles and the neutrinoless double beta decay ($0\nu\beta\beta$) [49, 50].

2.1.1. DARWIN baseline design

The DARWIN detector will consist of a low-background double-walled cryostat which will hold the large volume of liquid xenon. The cryostat will be surrounded by concentric shielding structures. At the core of the experiment, there is a dual-phase TPC which is 2.6 m tall and 2.6 m in its diameter containing the active xenon mass. Arrays of photosensors will be installed above and below the liquid xenon target to detect prompt and delayed VUV scintillation signals. In order to drift the electrons from the interaction vertex, a drift field of $\mathcal{O}(0.5)$ kV/cm across the liquid xenon target is required. This will be achieved with the help of field shaping rings made from oxygen-free high conductivity (OFHC) copper, optimised for such high voltages in order to ensure field homogeneity across the cathode and the anode. A high voltage feed-through will be passed into the TPC to reach the cathode at the bottom. PTFE reflectors will be suitably placed to ensure the VUV do not escape before reaching the photosensors. A drawing of the above mentioned components of DARWIN is shown in figure 2.1.

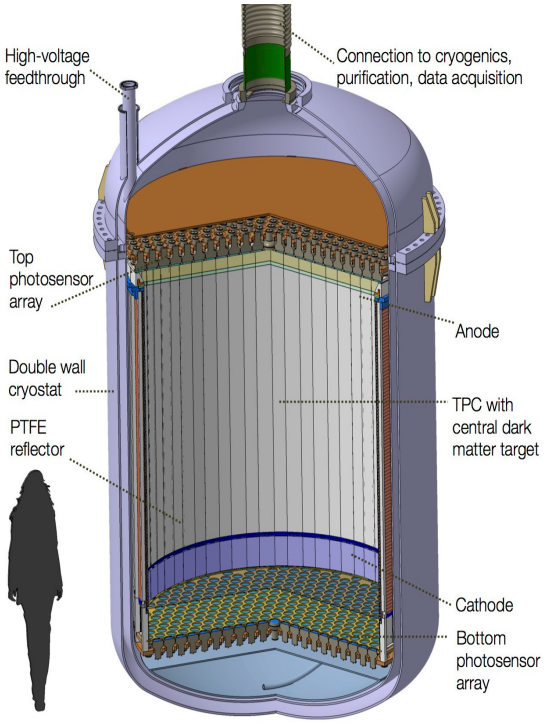

Figure 2.1.: *A possible realisation of a 50 t (40 t) total (target) LXe mass DARWIN detector. Image taken from Ref.[42].*

2.1.2. Challenges

The construction of such a large LXe TPC will give rise to several challenges. Most of them are studied within the rich R&D programme of DARWIN. Some challenges in the design R&D for DARWIN include: application of high voltage across the 2.6 m length, design of the purification system to improve the light collection yield, achievement of a low energy threshold and a good signal-background discrimination. Novel photosensors like silicon photo multipliers (SiPMs), Silicon Geiger Hybrid Tube (SiGHT) or gaseous photo-multipliers as a replacement for the photomultiplier tubes (PMTs) are also being considered.

In order to address some of the design challenges, a 2.6 m tall demonstrator is being built in the Physics Department at the University of Zurich. The motivation and description are detailed in the next section.

2.2. The 2.6 m tall TPC demonstrator

The 2.6 m tall demonstrator is a prototype experiment for DARWIN in the vertical direction. It will hold a total of $\sim$ 350 kg of LXe with $\sim$ 142 kg in the TPC.

Figure 2.2 is a rendering showing the cross section of the TPC, cryostat along with the support structures of the 2.6 m tall demonstrator

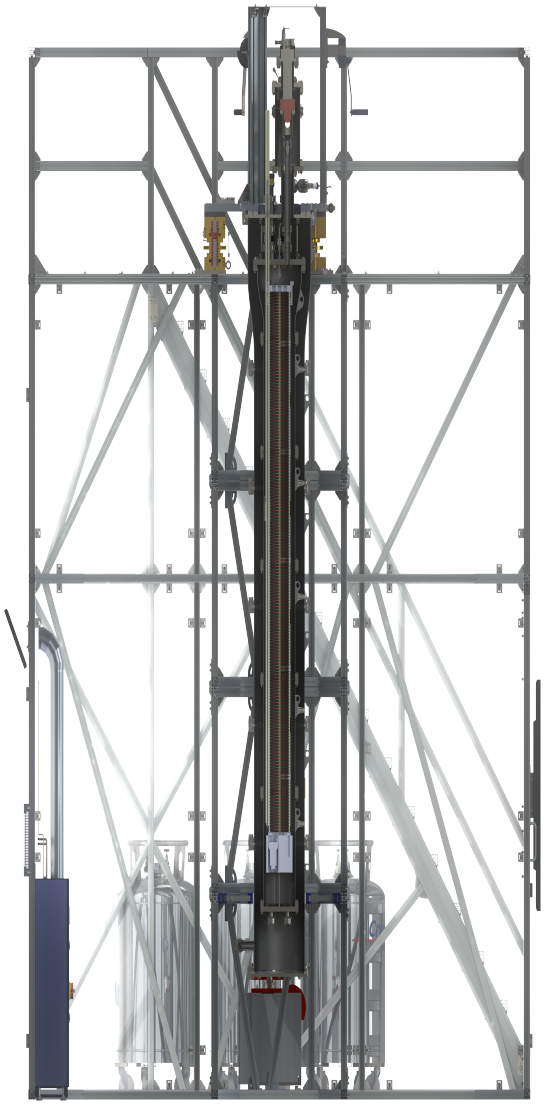

Figure 2.2.: *Model of cross section of the demonstrator cryostat and TPC [51].*

2.2.1. Goals of the 2.6 m tall demonstrator

The main goals of the demonstrator are listed below:

- **Electron drift length**: The demonstrator aims to measure the electron drift across its 2.6 m height. This would be the largest ever attained electron drift length in LXe. This amounts to an average drift time of 2 ms for the electrons produced in LXe to reach the anode.
- **Purification system**: To enable the electron drift across the large length, it is necessary to have a fast liquid xenon circulation system. The circulation system will also include the xenon purification system which aims to purify the liquid xenon from its electro-negative impurities at a fast rate.
- **High voltage system**: Generation of a uniform electric field to achieve the

electrons drifting across the 2.6 m length requires a dedicated high voltage source generating a voltage difference of $\sim$ 50 kV and a field strength of $\sim$ 19.23 kV/m across the TPC.

2.2.2. TPC construction

The demonstrator will be housed inside a support structure whose frames are made from aluminium profiles. This support structure (figure 2.3) will serve as clean room, walls, top floor and lateral support to the inner frames, which bears the weight of the demonstrator. A double walled stainless steel cryostat which is 3.5 m tall is placed inside the inner frame of the support structure with the help of a leveling system. The inner cryostat will be filled with LXe, whose circulation and purification is managed by a gas system. A 2.6 m tall dual-phase TPC with a radius of 8 cm will be placed inside the inner cryostat.

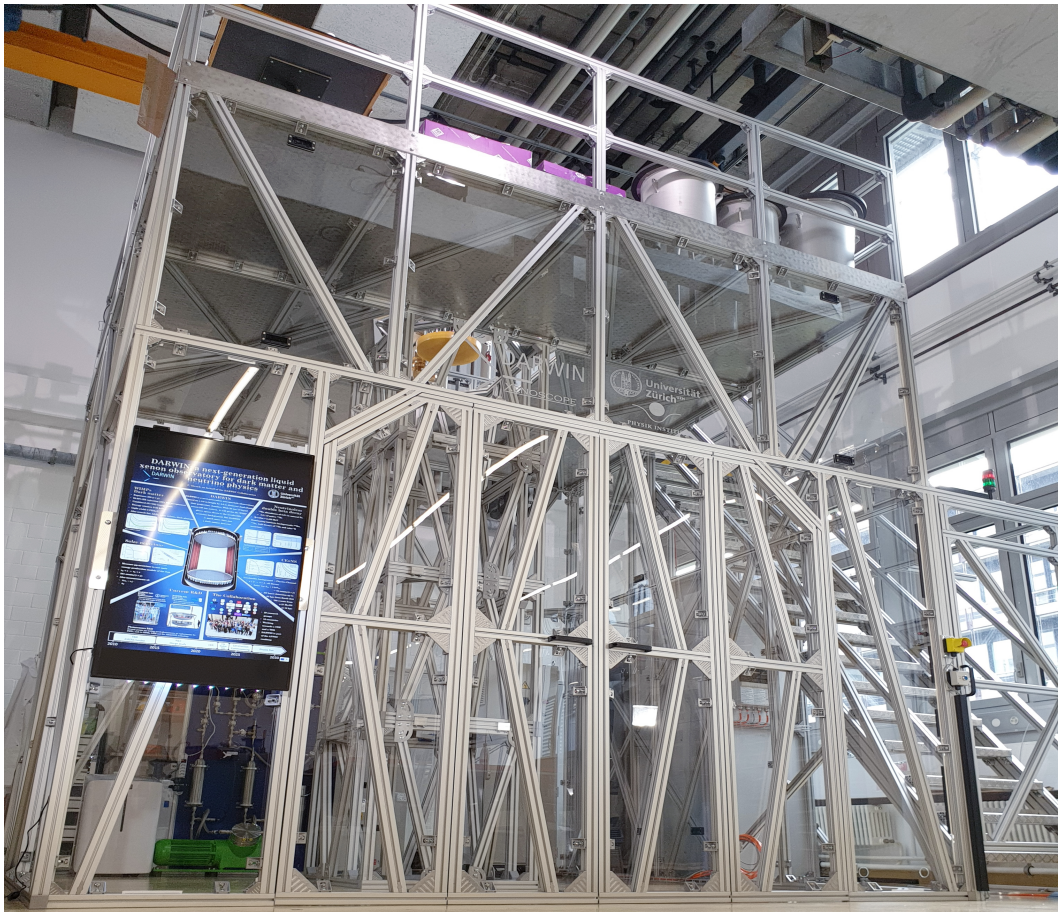

Figure 2.3.: *Support structure of the demonstrator constructed at the assembly hall of UZH, Irchel campus. [51]*

The main constituents of the TPC are described in the following list:

- **Field shaping rings**: Field shaping rings made from OFHC copper would be placed along the TPC in order to establish a high voltage difference across

the 2.6 m length to ensure field uniformity.

- **Cathode and anode mesh**: A cathode mesh is placed near the bottom of the TPC, a few centimeters above the PMT arrays. An anode mesh is placed in the GXe phase right below the SiPM array.
- **High voltage supply**: A high voltage power supply is necessary for the generation of uniform electric field across the TPC.
- **Reflectors**: Polytetraflouroethylene (PTFE) reflectors are suitably placed to ensure that the VUV photons generated inside the TPC do not escape and can travel towards the photosensors.
- **Photosensors**: The demonstrator will be equipped with an array of VUV-sensitive PMTs at the bottom, an array of SiPMs on the top and SiPM rings along the TPC cylinder. These will be held in place with the help of PTFE holders. A detailed description of the photosensors and its arrangement is provided in the next section.

2.2.3. Photosensors

Photomultiplier Tubes (PMTs)

The Hamamatsu R11410-21 PMT is the photodetector of choice for the demonstrator bottom array. The device has been optimized for a very low intrinsic radioactivity, a high quantum efficiency at 178 nm and a high sensitivity to single photon detection. A picture of the inside of the PMT is shown in figure 2.4. Two such PMTs will be assembled at the bottom of the demonstrator TPC.

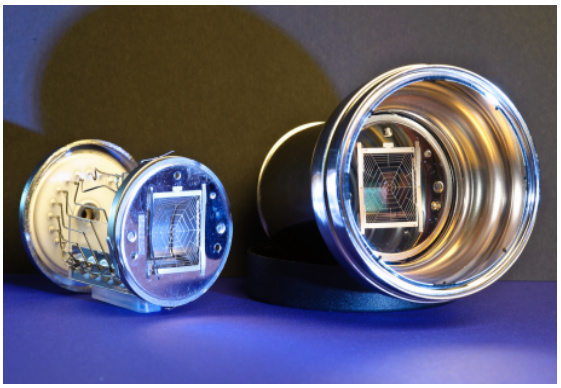

Figure 2.4.: *Hamamatsu R11410-21 PMT*

Silicon Photomultipliers (SiPMs)

The SiPM S13370 series is a Multi-Pixel Photon Counter (MPPC) for VUV light detection that is suitable for detecting scintillation light of LXe. An array of such SiPMs will be arranged at the top of the demonstrator TPC. SiPM arrays in dual

phase TPCs was previously tested in an experiment Xurich, where their characteristics was studied in LXe medium [52]. A rensdering of one SiPM preamplifier unit is shown in figure 2.5

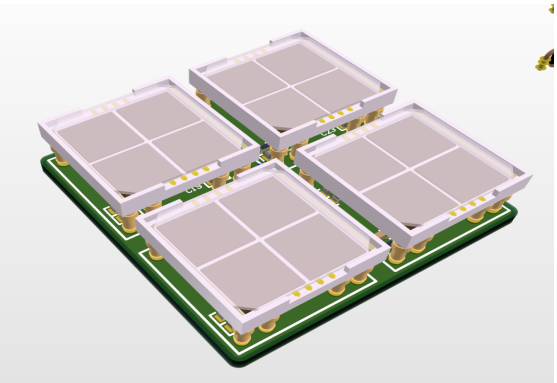

Figure 2.5.: *One SiPM preamplifier unit [53]*

2.2.4. Motivation for simulation requirements

Due to the smaller radius of the demonstrator TPC, VUV light produced near the center of the TPC does not entirely reach the photosensors placed at the top and bottom ends. In order to surpass these geometrical constraints, the TPC must have photosensors along its cylindrical surface in addition to those on the top and bottom. Some challenges in the TPC design include optimizing the placement of SiPM rings. This is a specific challenge as these rings would be near the high electric field regions of the field shaping rings. Performing light collection efficiency (LCE) simulations is the way to approach this problem and maximize the efficiency of the TPC. The LCE simulations and the conclusions from the work are discussed in the next chapter.

3. Light Collection Efficiency Simulations

As described in the previous chapters, a dual-phase TPC will observe a detection when scintillation photons are produced in the liquid or when accelerated electrons produce photons in the gas phase. In the case of the 2.6 m tall demonstrator, electrons drifted vertically will be extracted from the liquid phase and accelerated in the gas phase resulting in a scintillation signal collected by the array of SiPMs placed at the top of the TPC. The electrons are collected at the anode. Photons generated will be collected by both the SiPMs at the top and PMTs at the bottom. As a result of Rayleigh scattering, absorption by impurities in the liquid, PTFE and other TPC materials, photons produced near the centre of the TPC are significantly attenuated by the time they reach the photosensors on both ends. The photon intensity is further diminished by the thin cylindrical geometry of the demonstrator. The capacity of the TPC to collect photons is quantified by its 'light collection efficiency' (LCE) which is the ratio of intensity of detected photons to the intensity of generated photons. An optimal dual-phase TPC designed for dark matter detection should have a geometry and light detection scheme that maximizes its light collection efficiency.

In an attempt to improve the LCE of the demonstrator, PTFE reflectors and rings of SiPM are introduced into the TPC. The challenge now arises about the choice of the placement of PTFE reflectors, rings, and also about the number of rings and SiPMs required. In order to address this challenge, simulations for different design configurations are performed and LCE values for each configuration are obtained.

The following sections of this chapter discuss the simulation procedure and results. The simulations were performed using the GEANT4 package which is discussed in section 3.1. Modelling of the geometry and its visualization is detailed in section 3.2. LCE simulations are discussed in section 3.3

3.1. GEANT4

GEANT4 [54] is a C++ based Monte Carlo (MC) code originally developed at CERN. This package can be used for geometry construction, simulating the passage of particles through matter, incorporating physics models and recording hits. It finds its applications in particle and astroparticle physics, nuclear physics, accelerator design, space engineering and medical physics.

In this project, GEANT4 is used to construct the TPC geometry and simulate events within the liquid xenon target volume and observe the LCE of the TPC for different design configurations. The results of the simulations are obtained in the form of a ROOT file. The ROOT file data is analysed with Python 3 using the Uproot package available for Python [55].

GEANT4 comprises the following modules:

- **Geometry construction**: This module involves the construction of geometry of the demonstrator. It is written by defining individual parts and their materials.
- **Physics definitions**: The physics processes required for the simulations such as the nature of the particle source, parameters affecting the scintillation process, etc., are defined.
- **Detection recording**: The detectors are defined as sensitive volumes. A detection is recorded when an event occurs within the sensitive volume.
- **Events execution**: Events occurring are stored in ROOT files. In this case, the position, energy, momentum and the processes involved in the event generated are suitably processed and stored.
- **Messenger**: Messenger files allow for dynamical manipulation of parameters used in code.

The code execution format is summarised in the figure 3.1

3.2. Geometry Modelling and Visualization

GEANT4 has its own indigenous virtual particle called a *geantino*. Geantino is a chargeless, massless, completely non-interacting particle and it can be used for geometry and tracking diagnostics.

This can be suitably exploited in order to verify the geometry definitions and verify that it has no overlaps/errors. Geantinos are only transported through the confined volume and do not interact with any material. Hence the simulation is run at a time by confining the geantino production to one particular material, e.g., copper (field shaping rings) or stainless steel (cryostat).

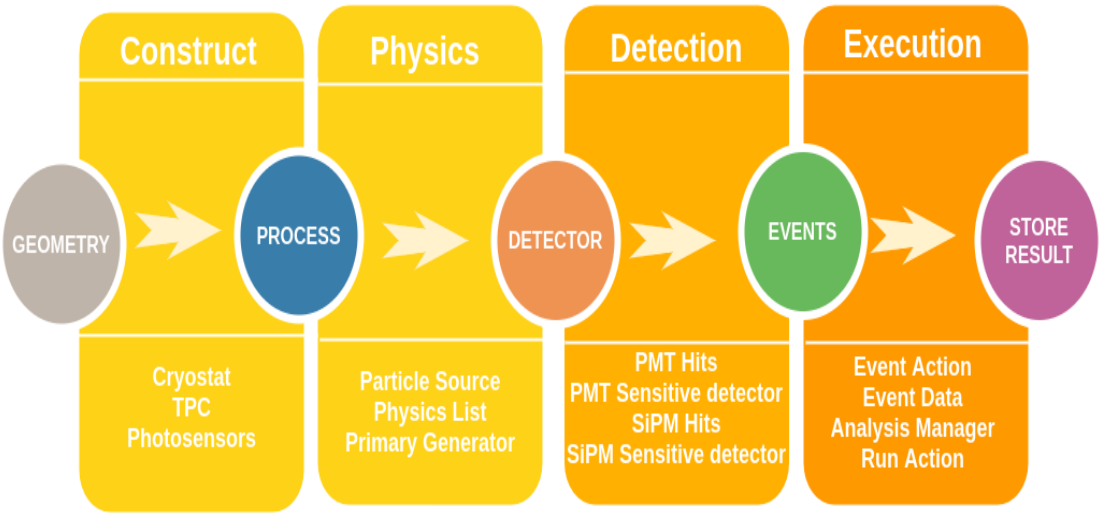

Figure 3.1.: *Flowchart showing the overall GEANT4 simulation process*

The geometry for the demonstrator is constructed using GEANT4 in 2 main classes, one for the cryostat and the other for TPC construction.

Cryostat modelling: A simplified version of the cryostat is constructed and the corresponding geantino simulation result is shown in figure 3.3. It comprises an outer and an inner vessel made up of stainless steel. There is vacuum in the space in between the inner and outer vessel.

TPC modelling: The geantino simulations for the dual-phase TPC construction is shown in figure 3.2 and figure 3.3. The inner vessel of the cryostat is filled with liquid xenon and gas xenon (of height 23 cm on top of liquid xenon). The TPC also consists of field shaping rings, PMTs, SiPMs and PTFE pillars and holders for support.

Photosensor modelling: A simple geometry of photosensors is implemented. In the bottom of the TPC, with a PTFE disk as a holder, two disks made up of PMT material are placed. On the top PTFE disk, 26 SiPMs are placed.

Once the geometry definitions are verified and visualized, we proceed towards performing light collection efficiency simulations discussed in the following sections.

3.3. Light Collection Efficiency

As discussed previously, the demonstrator requires SiPM rings along the TPC in order to efficiently detect photons from events occurring across the entire active volume of the TPC. A rendering of one SiPM ring with SiPMs placed outside the field shaping rings is shown in figure 3.4. A SiPM array can have multiple SiPM units embedded. One of the challenges involves deciding whether to place PTFE reflectors inside the TPC. This does improve the light collection efficiency,

but contributes to the contamination of liquid xenon due to the degassing of the molecules absorbed inside the PTFE material. This can lead to light attenuation by absorption on the released molecules. The next challenge would be to decide the number of rings and the specifications of SiPMs required.

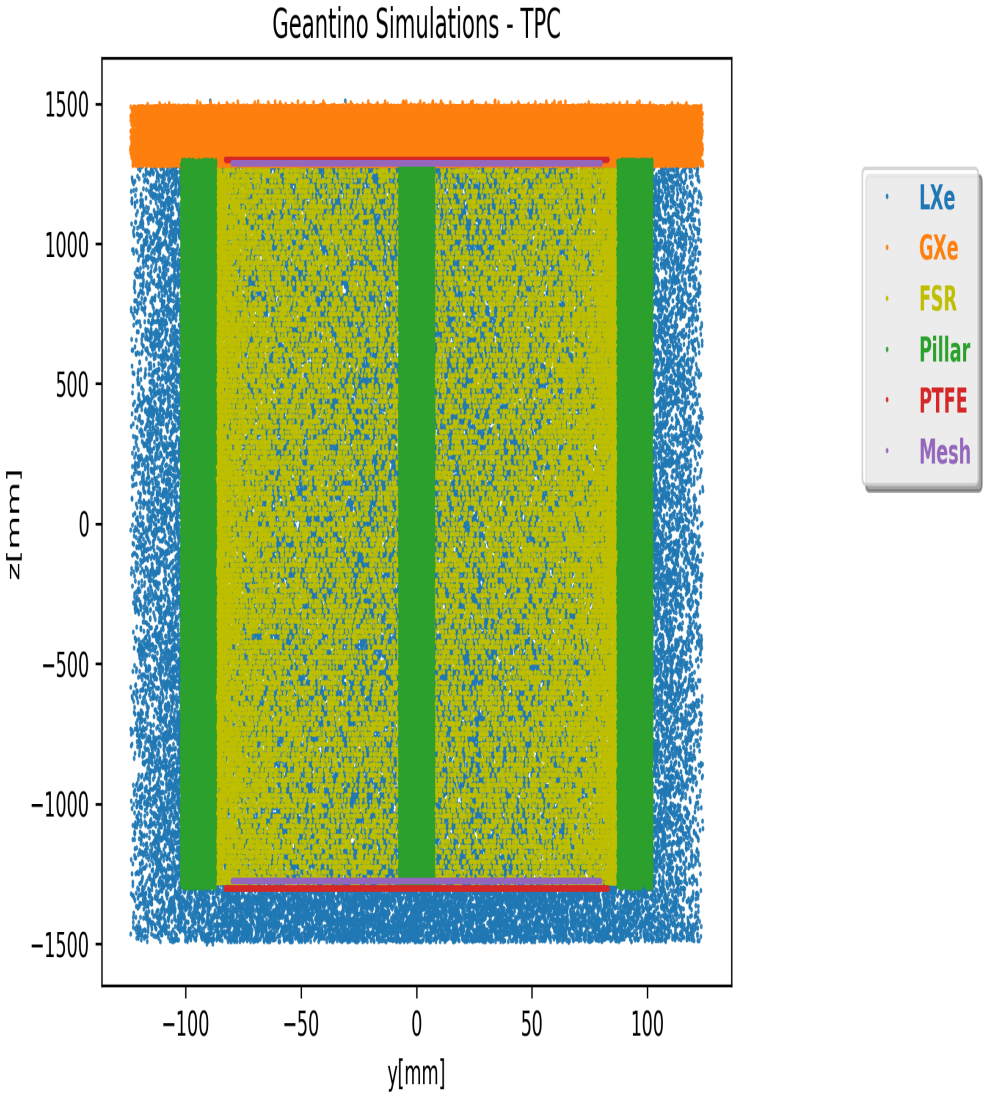

Figure 3.2.: Geantino simulations of TPC components. Simulations were run by confining geantinos to each component - LXe, GXe, field shaping rings (FSR), pillars, PTFE and meshes.

In order to address these questions, light collection efficiency simulations are performed for different configurations of the TPC design. The first question at hand was addressed by performing LCE simulations with and without PTFE in the TPC. An analytic estimation was made as shown in section 3.3.1, which was later compared with simulation results.

The light collection efficiency of the detector as a function of vertical height h is defined as follows:

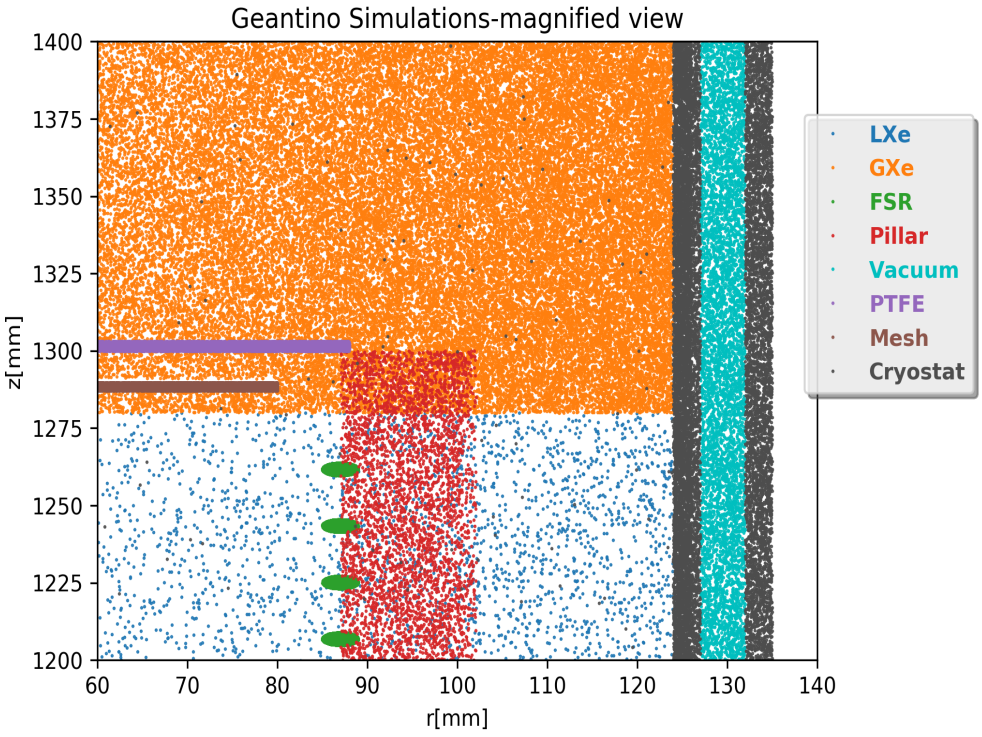

Figure 3.3.: *Geantino simulation results of TPC and cryostat geometry- magnified view*

$$\eta(h) = \frac{N_d(h)}{N_g(h)} \tag{3.1}$$

where $\eta(h)$ is the light collection efficiency at a height h, $N_g(h)$ is the number of photons generated at a height h and $N_d(h)$ is the number of photons detected by all the photosensors.

3.3.1. Analytic Estimate of Light Collection Efficiency

In order to validate the simulations, an analytic calculation was performed for later comparisons. A schematic of the TPC used for the estimation is shown in figure 3.5.

Photons that are generated at a height h from the bottom of the TPC undergo multiple reflections in the presence of PTFE reflector. They also undergo exponential attenuation in the LXe medium en route to the photosensors. The photon intensity is further reduced as a result of the transmittance factor associated with the PMT and SiPM windows. Photons reaching the top SiPM array undergo refraction at the LXe-GXe interface resulting in the reduction in intensity due to total internal reflection. Towards the end, the photon detection efficiency of the photosensors itself must be taken into account while converting the output signal to the actual intensity.

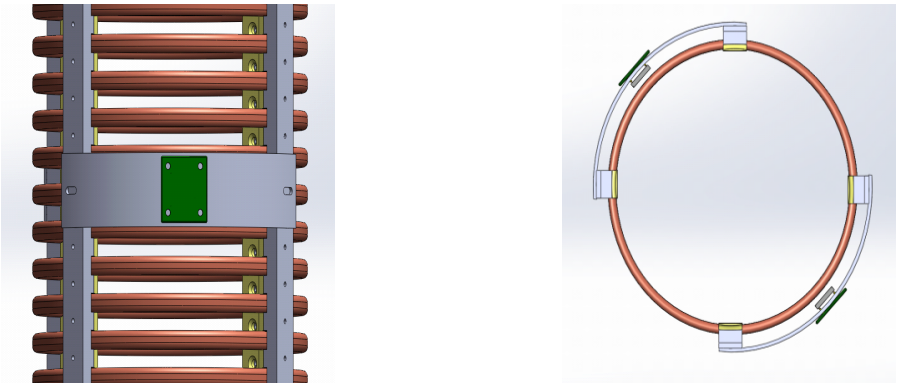

(a) (b)

Figure 3.4.: A rendering of SiPM ring placed outside the field shaping rings. a) Side view b) Top view.

The factors that contribute to the light collection efficiency estimation are listed in table 3.1.

Factors	**Parameter**	**Value**
Solid angle	Ω	$[0, 4\pi)$
Attenuation length	L_a	10 m
Rayleigh scattering length	L_r	40 cm
Ratio of indirect photons to direct photons reaching the photosensors	k	$(0, 1)$
LXe-PMT window transmittance	T_1	~ 0.8
LXe-GXe interface transmittance	T_2	~ 0.8
GXe-SiPM window transmittance	T_3	~ 0.8
Photon detection efficiency of PMT	Q_{PMT}	$\sim 28\%$
Photon detection efficiency of SiPM	Q_{SiPM}	$\sim 24\%$
Fraction of surface area of bottom disk sensitive to photons	A_{PMT}	0.32
Fraction of surface area of top disk sensitive to photons	A_{SiPM}	0.783

Table 3.1.: *List of factors affecting the light collection efficiency of the TPC.*

With all the factors mentioned in table 3.1 taken into account, the light collection efficiency as a function of height from the bottom of the TPC is given by the following equation [56]

$$\begin{aligned}\eta(h) = (1 + k(h))T_1 Q_{PMT} A_{PMT} \frac{\Omega(h)}{4\pi} \exp(-\frac{h}{L}) \\ + (1 + k(H - h))T_2 T_3 Q_{SiPM} A_{SiPM} \frac{\Omega(H - h)}{4\pi} \exp(-\frac{H - h}{L})\end{aligned} \tag{3.2}$$

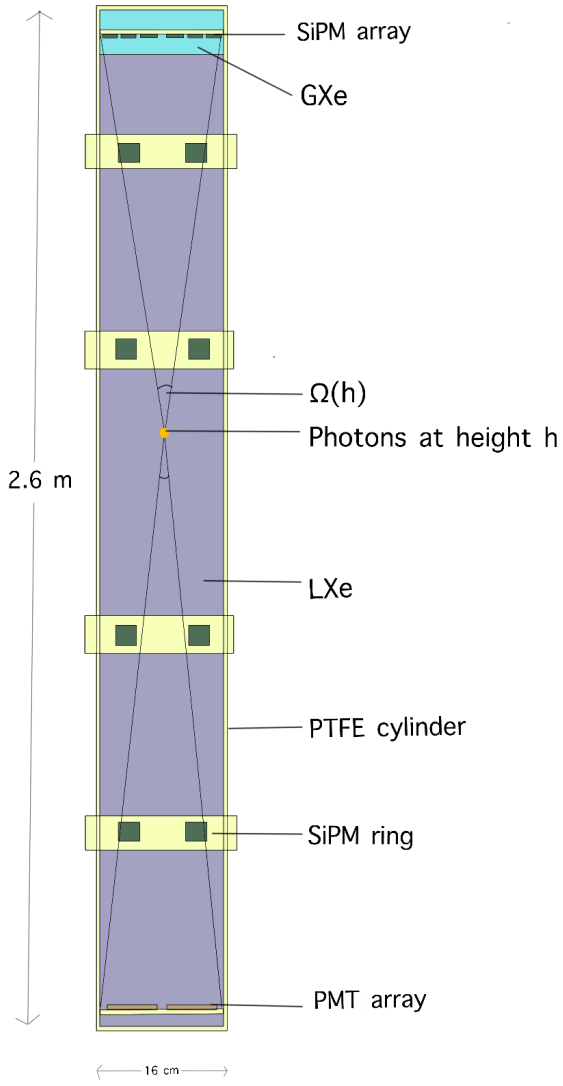

Figure 3.5.: *Schematic [not to scale] of demonstrator TPC used for estimating LCE.*

The function $k(h)$ can be estimated by taking into account the number of reflections undertaken by the photons before reaching the photosensors. The number of reflections (n) undergone affects the solid angle associated with the the fraction of total photons reaching the top and bottom. This equation takes into account the area, photon detection efficiency, solid angle and attenuation length for the top and bottom photosensor arrays.

The number of reflections undergone by the photons before it reaches the PMTs is $\leq n$, the solid angle that reaches the bottom would be:

$$\Omega(h) = \frac{1}{4}(1 - \cos\alpha_1) + \frac{1}{4}(1 - \cos\alpha_2) \tag{3.3}$$

Where,

$$\alpha_1 = \tan^{-1}\left[\frac{(2n+1)R + r}{h}\right] \tag{3.4}$$

$$\alpha_2 = \tan^{-1}\left[\frac{(2n+1)R - r}{h}\right] \tag{3.5}$$

Integrating this over a disk element at a height h and simplifying the obtained result, we get (the integration procedure is detailed in appendix A):

$$f(h) = 1 - 4h[\frac{(2n+1)^2 - 1}{\sqrt{h^2 + 4(2n+1)^2R^2} + 2(2n+1)R + h}] \tag{3.6}$$

Here $f(h) = \int_{disk} \Omega(h)$.

The final expression for LCE with fitted parameters (refer table 3.2) accounting for transmission coefficients is given by the following expression:

$$\begin{aligned} LCE(h) = (a \cdot A_{SiPM} \exp[-(H-h) \cdot (\frac{1}{L_r} + \frac{1}{L_a} + \frac{1}{L_t})] f(H-h) \\ + b \cdot A_{PMT} \exp[-h \cdot (\frac{1}{L_r} + \frac{1}{L_a})] f(h)) \cdot 100 \end{aligned} \tag{3.7}$$

3.3.2. Simulation Procedure

Once the geometry and the physics processes are defined in the GEANT4 code, we proceed with running the simulations. VUV photons are generated isotropically in LXe inside the TPC. The different steps followed in running the simulations are:

Fitted Parameters	
Number of reflections (n)	15
a	0.8
b	0.8
Transmission contribution L_t	57cm

Table 3.2.: *Parameters used in analytic fit*

1. The LCE is obtained without the PTFE reflectors.
2. A PTFE cylinder is inserted such that it is contained inside the field shaping rings and spans the entire length of the TPC. The LCE is then obtained.
3. A ring of height equivalent to SiPM is subtracted from the PTFE cylinder and its radius is increased to 9.0 cm such that this part is now outside the field shaping rings. SiPMs are mounted on this smaller ring. The LCE is obtained for various configurations by varying the number of rings and SiPM units per ring.
4. Instead of subtracting a ring as in (3), SiPMs are flushed onto the PTFE cylinder and arranged in the form of rings. The LCE is calculated for different configurations of SiPMs flushed onto the PTFE.

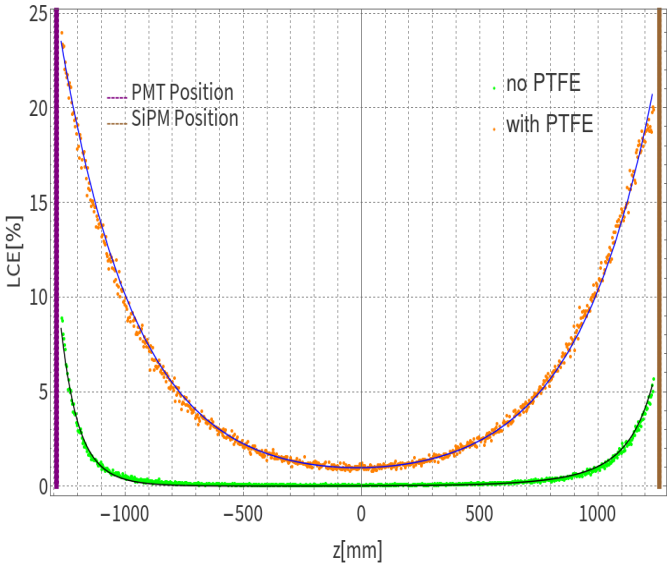

Figure 3.6.: *The LCE as a function of the height of the TPC. The bottom PMTs are placed at z = -1300 mm while the top SiPM array is placed at z = 1300 mm in the GXe phase. The blue curves are analytically estimated results.*

The overall LCE for the case with PTFE is 5.7% and the overall LCE for the case without PTFE is 0.6% and is validated by the analytic results as can be seen in figure 3.6. This shows that there is a significant improvement in the light collection efficiency in the presence of PTFE. Hence, further progress with the

design optimization was carried out by keeping the PTFE cylinder intact inside the TPC.

3.4. SiPM Rings

From figure 3.6 we can see that even with the PTFE cylinder inside the TPC, the LCE near the centre of the TPC is very low i.e., $< 1\%$. Hence, in order to be able to efficiently detect events occurring near the centre of the TPC, the placement of rings of SiPMs was proposed. Initial simulations with SiPM rings placed outside the field shaping rings showed that the improvement to the overall LCE was negligible. SiPM rings inside the field shaping rings (flushed along the PTFE cylinder) showed significant improvement. The LCE plots for different configurations are shown in figure 3.7 and table 3.3 lists the percentages averaged over the entire length of the TPC, of the overall LCE for each configuration that is plotted. Notice that the data appears to be broadened vertically with increase in number of SiPM units per ring. This is due to the LCE having a larger peak at points where the rings are placed and this peak's height increases with increase in the number of SiPMs.

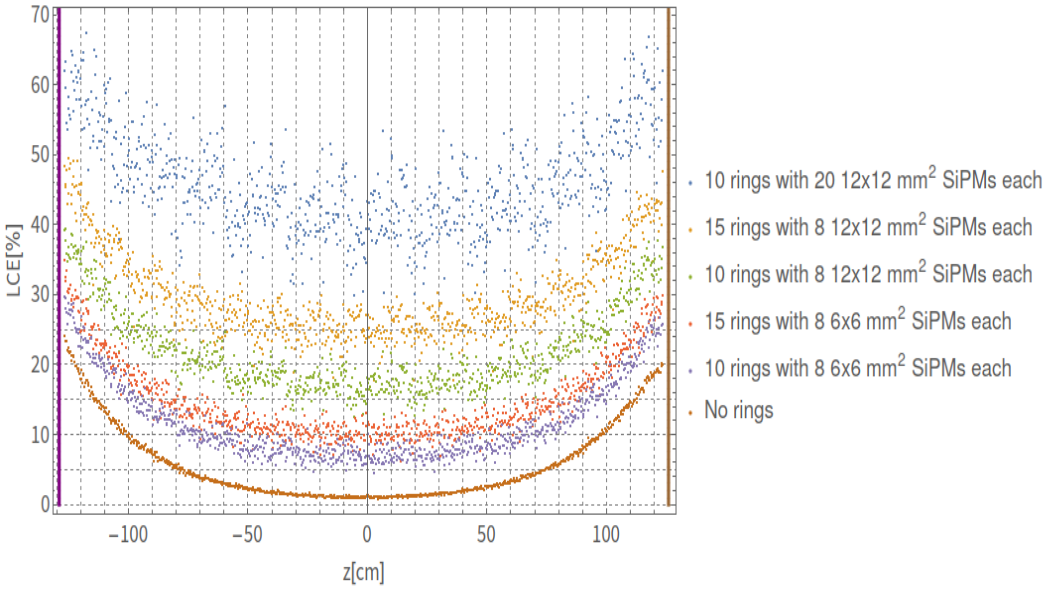

Figure 3.7.: *Light collection efficiency as a function of the height of the TPC. The bottom PMTs are placed at z = -130 cm while the top SiPM array is placed at z = 130 cm in the GXe phase. The SiPM rings are placed such that they are flushed onto the PTFE*

# Rings	SiPM area[mm^2]	# SiPMs/ring	LCE[%]
10	12	20	45.75
15	12	8	29.74
10	12	8	21.74
15	6	8	14.73
10	6	8	11.73
0	-	-	5.73

Table 3.3.: *Overall average LCE % for each configuration*

3.5. Conclusion

We can conclude that the case with 10 rings having twenty 12×12 mm^2 SiPM units each yields a $\sim$ 50% LCE as compared to the case with 10 rings with eight 12×12 mm^2 SiPM units, which gives $\sim$ 25% efficiency. While having a maximum number of SiPMs and rings largely enhances the overall LCE of the TPC, realizing them in the demonstrator TPC poses challenges such as increasing the number of readout channels, hence complicating the trigger signal. Running the readout cables of the SiPM across the TPC in presence of the field shaping rings set at high voltage poses a risk of an electrical short as well as the readout signal itself getting modified due to the presence of strong electric fields ($\sim 19kV/m$). Hence, the aim is to minimize the number of SiPMs while maintaining an optimal LCE. Hence a discussion on the minimum number of SiPMs required is presented in chapter 5.

4. Experiment to test the Silicon Photomultiplier field of view

In an attempt to understand the hardware instrumentation setup associated with photosensors, an experiment to test the field of view of a single SiPM unit was carried out. The results of this experiment helped us verify the behaviour of the LCE as function of distance of the photon source from the SiPM. A description of the workings of the SiPM that was used for testing is given in the following section.

4.1. Silicon Photomultipliers

Silicon is one of the most important materials in semiconductor devices. The ability for silicon to be doped with various impurities results in its excellent capabilities in transport of holes and electrons. Doped silicon is mainly used in the preparation of diodes and transistors.

Silicon photo multipliers (SiPMs) are solid-state single photon sensitive devices. Absorption of a photon by an SiPM can produce a current pulse several tens of nanoseconds long containing 10^5 to 10^6 electrons. This amplification of a photon signal into a large electron current signal is called *gain* of the SiPM and this is comparable to that of photo multiplier tubes (PMTs).

An SiPM is comprised of multiple microcells or *pixels*. A single pixel is nothing but a series combination of an avalanche photodiode (APD) and a quenching resistor (R_Q). All the microcells are connected in parallel as depicted in figure 4.1. In the end, a SiPM will have two ports: an anode and a cathode.

Commercial SiPMs have identical microcells with its size varying from 10 μm to 100 μm arranged in a rectangular pattern. There can be hundreds to tens of thousands microcells per SiPM. The spectral sensitivities of SiPM range from UV to IR peaking at the visible range (400 nm-500 nm).

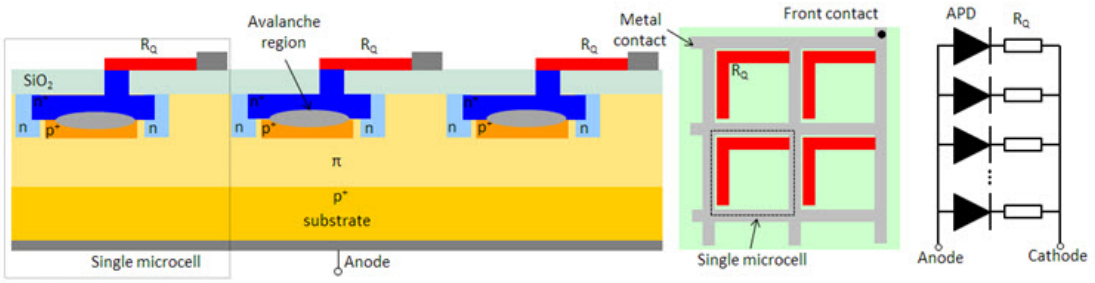

Figure 4.1.: *This figure depicts a typical structure of an SiPM. From left to right: a cross section of 3 microcells, top view with 4 microcells and the arrangements of APDs and quenching resistors. Adapted from [57]*

4.1.1. Avalanche Photo Diode (APD)

An avalanche photodiode (APD) is a highly sensitive semiconductor photodiode that exploits the photoelectric effect to convert light into electricity.

When light enters an APD, electron-hole pairs are generated if the light energy is higher than the band gap energy. The carriers generated are multiplied in an APD unlike that in a normal photodiode. When electron-hole pairs are generated in the depletion layer of an APD with a reverse voltage applied to the PN junction, the electric field causes the electrons to drift toward the N^+ side and holes drift towards the P^+ side. When the reverse bias voltage is increased beyond a certain threshold, the generated carries collide with the crystal lattice creating new carriers as a result of ionisation. The newly generated carriers accelerate and further generate newer carriers. This cycle is called *avalanche multiplication* depicted in figure 4.2. Gain of the APD is proportional to reverse bias voltage.

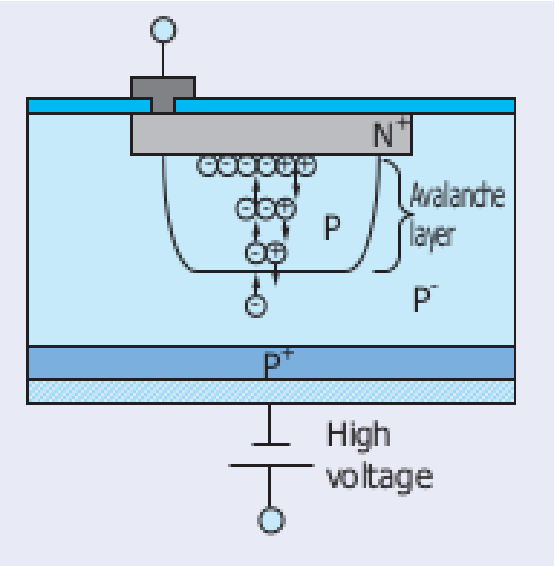

Figure 4.2.: *Principle of APD operation. Figure adapted from [58]*

The multiplication factor (M) for an APD is given by the following expression:

$$M = \frac{1}{1 - \int_0^L \alpha(x)dx} \tag{4.1}$$

Where L is the space-charge barrier for electrons and α is the multiplication coefficient as a function of displacement x.

APDs are more sensitive compared to other semiconductor photodiodes as their gain can be strongly varied with the applied reverse bias voltage and temperature.

4.1.2. Working Principle of SiPMs

Once the APDs and quenching resistors are assembled to form multiple pixels, the entire SiPM is biased in such a way that the voltage on each APD is above its breakdown value (see figure 4.3). The APD hence outputs a pulsed signal every time it registers a photon in the form of a 'click'. This mode of operation of the APDs is called the Geiger-mode. The major parameter used to control the SiPM is the difference between the biasing voltage and the breakdown voltage known as overvoltage. After a photon triggers the avalanche process in the APD, the quenching resistor brings the APD back to the Geiger mode. Unlike CCDs, SiPMs do not store charge and it outputs an analog signal that can be measured in real time.

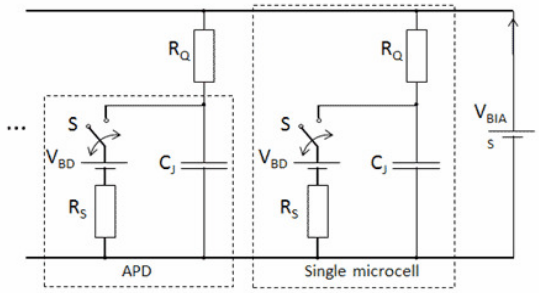

Figure 4.3.: *A simplified equivalent circuit of an SiPM (two representative microcells) biased with an external voltage source V_{BIAS}. Here C_J is the junction capacitance, V_{BD} is the breakdown voltage of the APD and S is the switch. Adapted from [57].*

4.1.3. The 6 × 6 mm^2 MPPC SiPM from Hamamatsu

The photosensor of interest in this experiment is the 6x6 mm^2 Multi-Pixel Photon Counter Silicon Photo Multiplier (MPPC SiPM). It is sourced from Hamamatsu manufacturers, who label this kind as the S13370/S13371 series. This series of SiPMs are specifically designed to be sensitive in the VUV region as can be ascertained from the photon detection efficiency plot shown in figure 4.4. It is mainly used for academic research purposes in particle detection experiments.

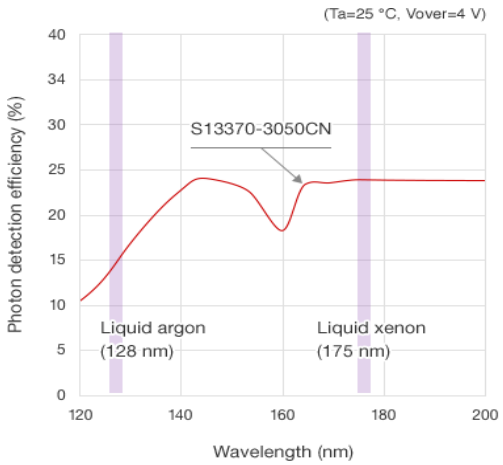

Figure 4.4.: *Photon detection efficiency of Hamamatsu SiPM. Plot taken from [59].*

The output of the MPPC is a superposition of signals from each pixel. Each pixel outputs only one pulse and this is constant regardless of the number of incident photons. As a result of this, the linearity of the output gets worse with the increase in the number of incident photons. When the incident photon number count is low enough ($\mathcal{O}(10)$), then the output of the MPPC can be converted into the number of incident photons. Figure 4.5 shows the output pulses for different number of incident photons, when a charge amplifier was used to amplify the output signals.

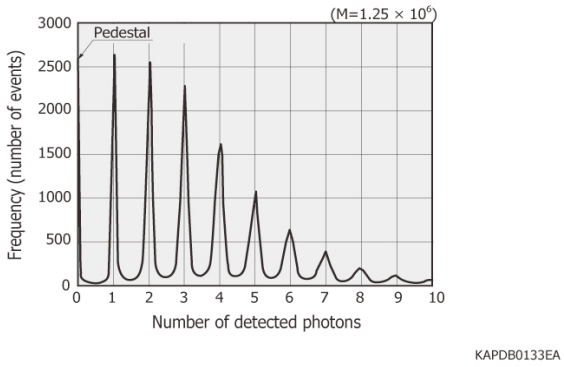

Figure 4.5.: *Pulse height spectrum when using change amplifier [60].*

4.1.4. Characteristics

Some important characteristics of the MPPC SiPM when compared to a photodiode, a single APD and a PMT are listed in the table 4.1. The ratio of the number of generated electron-hole pairs to the number of incident photons is defined as the quantum efficiency (η), expressed in percent (%).

The photon detection efficiency (ξ) is a probability that the SiPM produces an output signal in response to an incident photon. It is a function of overvoltage ΔV and wavelength λ of the incident light, and can be expressed as a product

	PD	APD	MPPC	PMT
Gain	1	10^2	10^6	10^7
Sensitivity	Low	Medium	High	High
Operation voltage	5 V	100 to 500 V	30 to 60 V	800 to 1000 V
Noise	Low	Middle	Middle	Low
Response time	Fast (ns)	Fast (ns)	Very Fast (ps)	Fast (ns)
Energy resolution	High	Medium	High	High
Temperature sensitivity	Low	High	Medium	Low

Table 4.1.: *Comparing characteristics of photo-diode (PD), APD, MPPC and PMT. [60]*

$\xi(\Delta V, \lambda) = f \cdot \eta \cdot P_G$. In the equation, f is a geometrical fill factor, η is the quantum efficiency, and P_G probability of Geiger discharge. The photon detection efficiency is thus a key characteristic of a SiPM.

4.2. Description of the Experiment

A PTFE sheet of thickness 3 mm was rolled into a cylinder of radius 8 cm (same as that of the demonstrator TPC). The length of the cylinder is 50 cm, Optimized to fit inside a black-box which is a light tight box. A square cavity of side length 6 mm was carved out with four holes for supporting screws, to make room for placing and adjusting the SiPM.

The outer surface of the cylinder was tightly wrapped with polyethylene adhesive tape so as to make the PTFE opaque from the outside and also mimic the placement of copper rings outside the PTFE similar to the demonstrator TPC. The two ends of the cylinder were sealed with plastic caps, one of them was removed for data collection in order to avoid reflections from the cap.

The cap on one end has two holes made as a provision to insert and control the LED. A blue LED emitting light at the wavelength of $\sim$ 475 nm was tied to the end of an aluminium rod. While the LED wavelength is different from that of VUV light, it does not affect the geometrical estimation of LCE. After marking a scale with a resolution of 1 cm, this rod was passed through the hole of the cap. The cap was finally closed and sealed to the cylinder, with room for adjustments for the aluminium rod.

A 6×6 mm^2 SiPM (figure 4.7a) was mounted across the surface of the cylinder. This entire setup was placed inside the black box as shown in figure 4.6 and the cables from SiPM and LED were connected to the outlets in the black box. The black box was finally closed after ensuring the environment to be light-tight. The SiPM cables were connected to a power source and the DAQ (Data Acquisition) system. The LED was connected to a pulse generator. Short square pulses with very short rise and fall times ($\sim$5 ns) were generated by the pulse generator. The

illumination of the LED was kept low enough to ensure the non-saturation of the SiPM.

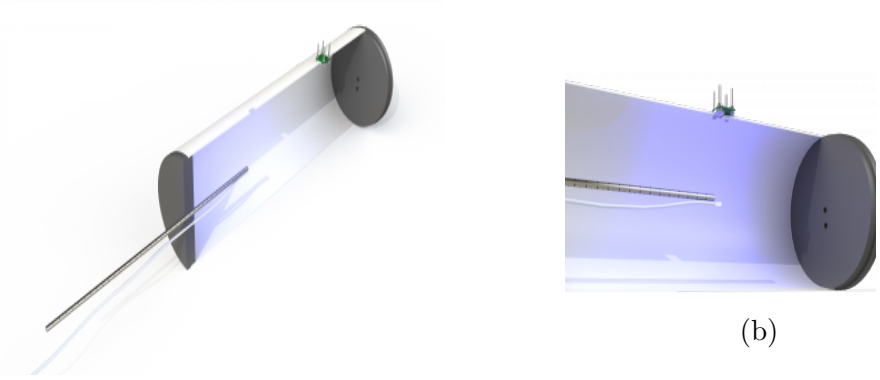

(a) (b)

Figure 4.6.: *Cross section view of the CAD diagram of the setup. a)PTFE cylinder closed with the lids and SiPM attached. b) Magnified view of (a) where the LED is at the nearest accessible point to the SiPM [?]*

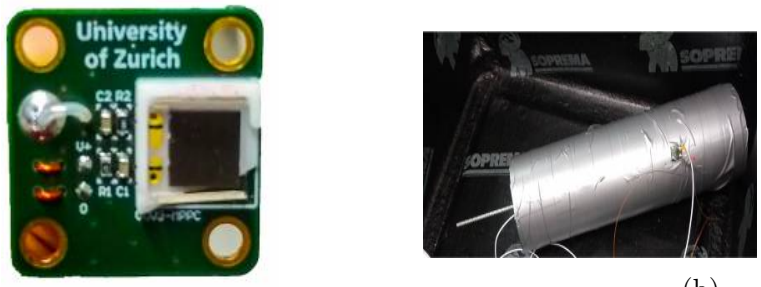

(a) (b)

Figure 4.7.: *a: 6×6 mm^2 SiPM used to test the its field of view inside the setup. b:Picture of the setup placed inside blackbox.*

4.3. Data Collection

After assembling the setup inside the black box, the pulse generator connected to the LED and the power supply to the SiPM were switched on (see figure 4.8 for the setup diagram). For each configuration of the setup, 10^5 events were recorded. The data was recorded in the form of ADC (Analog to Digital Converter) counts as shown in figure 4.9. A set of data was collected by varying the LED distances and the SiPM distance from the cylinder. Additional changes were made to the setup to enhance the data qualities in the following ways:

1. The LED light is anisotropic. Hence it was covered with Teflon tape in order to make the light isotropic.

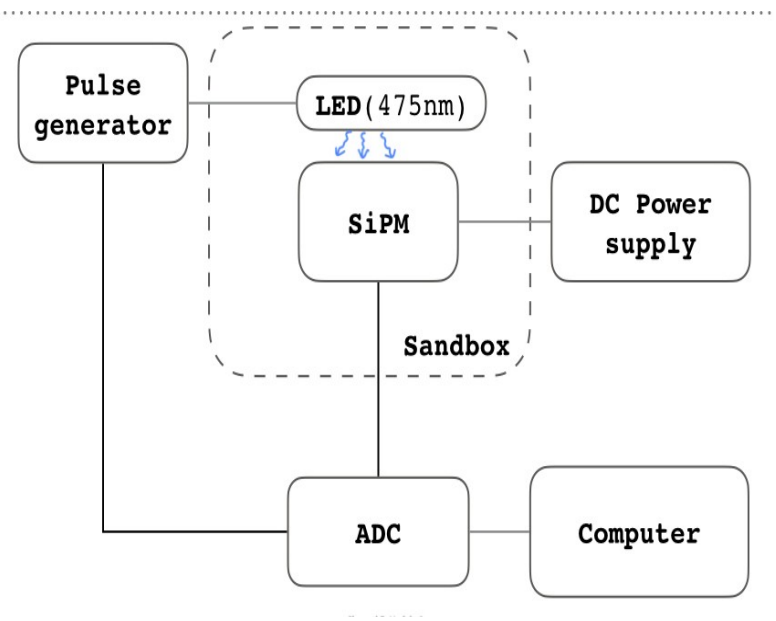

Figure 4.8.: *Setup schematic.*

2. The cap on the cylinder near the SiPM end was reflecting light. Hence this was completely removed.

3. The rod controlling the LED was free to rotate axially, which led to variations in the LED distance from the SiPM. Making additional marks on the rod helped to keep the axial configuration of the LED fixed.

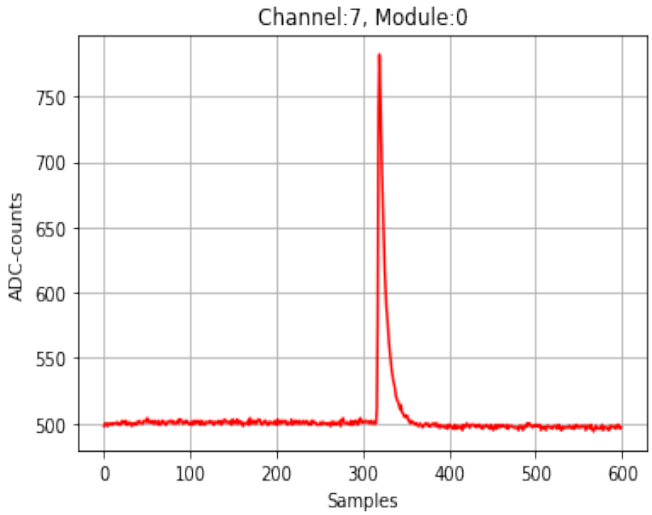

Figure 4.9.: *The recorded waveform for one event. The number of events collected per run was 10^5.*

4.4. Analysis

The mean peak area of the ADC counts recorded for each configuration was calculated and plotted as a function of distance of the LED from the SiPM for 3 different configurations of the SiPM placement. The initial configuration of the SiPM is referred to as the flushed configuration, where the exposed surface of the SiPM is aligned along the surface of the PTFE cylinder. The result for this arrangement are shown in green in figure 4.10. The next two sets of readings plotted in red and blue were taken with the SiPM 1 cm and 4 mm away (outwards) from the cylinder.

In figure 4.10, the error bars along x-axis was taken to be a constant of 0.5 cm as this was the resolution of the markings made on the aluminium rod. The error bars along the y-axis are the standard deviation of the peak-areas across 10^5 events.

In order to convert the ADC counts to photoelectrons, we use the following conversion:

$$\#\ \text{Photoelectrons} = \frac{\text{Voltage Bin} \times \text{Time Bin}}{\text{Resistance} \times \text{Elementary Charge} \times \text{Gain}} \tag{4.2}$$

The number of photoelectrons can be calculated by using the parameters given below.

Voltage Bin	$2.25\text{V}/2^{14}$
Time Bin	10^{-8} s
Resistance	50 Ω
Elementary Charge	1.602×10^{-19} C
Gain [61]	1.17×10^{6}

Table 4.2.: *Parameters used for converting ADC counts to photoelectrons*

A Gaussian was fit to a part of the data as shown in figure 4.10. The data significantly deviates from the Gaussian at large z due to geometrical effects of cutting a part of the PTFE cylinder to make space for the SiPM and also that the cylinder length is finite with one end contributing to reflecting photons. The Full Width Half Maximum (FWHM) of each of these Gaussian gives a quantitative measure of the field of view of the SiPM for different configurations as listed in table 4.3.

4.5. Results and conclusions

The motivation for performing this experiment was to provide an experimental support to the LCE simulations that were performed. The field of view for a

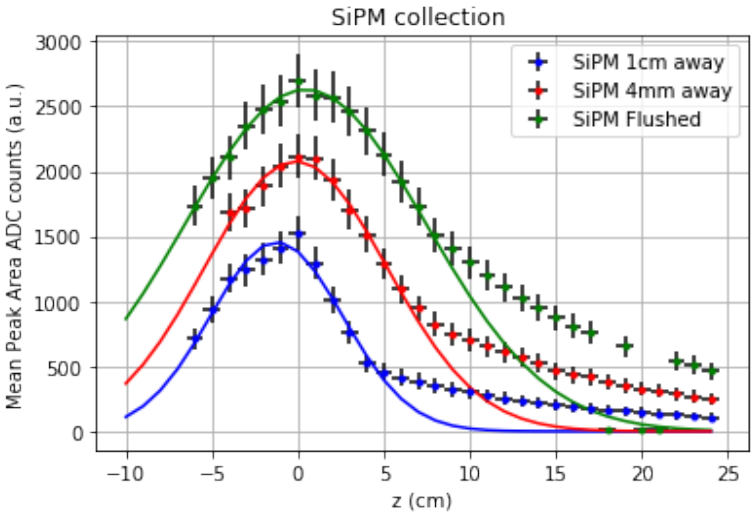

Figure 4.10.: *Peak area of the SiPM hits with LED wrapped with Teflon tape. The SiPM is placed at z=0 cm and readings are taken with position of LED spanning from -6 cm to 25 cm.*

single SiPM recorded in this experiment shows that a single SiPM flushed onto the PTFE cylinder has an average field of view of 16.5 cm at FWHM. And this decreases significantly with the SiPM being further away from the PTFE cylinder as can be seen from table 4.3.

The deviation of the data from the fitted Gaussian is later harnessed in chapter 5 where only part of the simulation data was fitted to a Gaussian knowing that data taken further away from the SiPM position is deviant from a Gaussian.

SiPM configuration	**FWHM**
Flushed	16.50 ± 0.16 cm
4 mm away	12.50 ± 0.28 cm
1 cm away	9.09 ± 0.26 cm

Table 4.3.: *FWHM values as obtained by the Gaussian fits to each data set.*

5. Simulating Electronic Recoil Signals from Radiogenic Sources

As discussed in chapter 1, a dual-phase xenon TPC records signals as a result of electronic and nuclear recoil (ER and NR, respectively) events occurring inside LXe. In a surface laboratory environment such as the one of the 2.6 m tall demonstrator, there is a constant flux of various particles that interact inside the TPC and can be characterized as background events.

An extensive study of potential background sources is necessary for dual-phase TPCs such that extremely rare events as expected from WIMP interactions are significantly distinguishable from background signals. In case of the 2.6 m tall demonstrator TPC, knowledge of background radiation signals is necessary in order to decide on a calibration strategy and a data acquisition (DAQ) setup.

In this chapter, different sources of background radiation are discussed in section 5.1. This section ends with the conclusion that concrete and stainless steel are the major contributors to the overall background rates.

An estimate of the rate of events occurring inside the TPC due to radiogenic impurities present in concrete is made in section 5.2. This estimate establishes the average rate that can be expected from MC simulation results, which is detailed in section 5.3. MC simulations were performed specifically for ERs occurring due to radiogenic impurities present in concrete and stainless steel materials. Results of the MC simulations are presented in section 5.4. Conclusions regarding the constraints posed on calibration sources by the background ER spectra are discussed in section 5.5.

5.1. Sources of Background Radiation

The different contributors to background signals are as follows:

- **Radioactive contaminants**: All materials used in the construction of the 2.6 m tall demonstrator and the components of the laboratory itself contain

radioactive isotopes that decay by emitting energetic particles. High energy γ particles produced lead to ERs as a result of Compton scattering and pair production. Radiogenic neutrons passing through the TPC lead to NR spectrum.

- **Atmospheric muons**: Cosmic-ray muons interacts with rock and concrete materials around the laboratory producing high energy neutrons. These muon-induced neutrons contribute to the NR spectra.
- **Intrinsic contaminants in xenon**: The major radioactive contaminants in xenon are ^{222}Rn and ^{85}Kr. β-decays occurring from these two contaminants also contribute to the ER spectra. Assuming that the procured liquid xenon is not purified, we can assume it is contaminated by natural krypton in ppb (parts per billion) [62]. The background signals from these intrinsic radioisotopes can be mitigated to a certain extent by the constant purification of xenon. Whereas in case of the 2.6 m tall demonstrator the purification system only separates electronegative impurities and hence ^{222}Rn and ^{85}Kr are not removed.
- **Solar neutrinos**: The constant flux of solar neutrinos produce ERs as they scatter off electrons of xenon atoms. NR spectra are also produced as a result of Coherent elastic Neutrino Nucleus Scattering (CNNS). In the case of the 2.6 m tall demonstrator, the background due to solar neutrinos is negligible due to their weak cross sections.

Among the above mentioned sources of background radiation, in this thesis we only explore ERs due to radioactive components in materials. A list of activities of different radioactive isotopes present in the materials is listed in table 5.1.

Source	^{235}U	^{238}U	^{226}Ra	$^{228}Ra(^{232}Th)$	^{228}Th	^{40}K	^{60}Co	^{137}Cs
Concrete	-	-	54.3×10^{3}	31.6×10^{3}	-	853.8×10^{3}	-	-
Stainless steel	4.2	150	4.0	5.4	4.5	5.6	37.9	1.5
Copper	0.15	2.4	7.3×10^{-2}	0.1	0.16	0.34	0.21	0.03
PTFE	8.7×10^{-2}	1.96	0.12	0.11	6.5×10^{-2}	0.34	2.7×10^{-2}	0.17
PMT	0.37	8	0.6	0.7	0.6	12	0.84	-
SiPM [52]	-	0.91	7.5×10^{-3}	9.2×10^{-3}	$6.6\text{x}10^{-3}$	2.6×10^{-2}	-	-
Aluminium [63]	1.3×10^{2}	6.5×10^{3}	8.3×10^{3}	1.6×10^{3}	$.9\text{x}10^{3}$	-	-	-

Table 5.1.: *List of activities for different materials in mBq/kg units except for PMTs given by mBq/PMT and for SiPM given by mBq/cm^2.*

Assuming the concrete walls whose dimensions are shown in figure 5.1, to be conventional i.e., containing CEM II/B cement [64], the radioactivity for this kind of concrete is taken from previous studies [65]. The assumption for radioactivity for stainless steel, copper and PTFE is taken to be the maximum values measured for the components used in the XENON 1T experiment [66]. In table 5.2 total mass and volume occupied by each material is listed.

^{226}Ra is the fifth daughter nucleus in the ^{238}U decay chain. Similarly, ^{228}Th is the third daughter nucleus in the ^{232}Th decay chain as seen in figure 5.2.

Upon observing the activities listed in table 5.1, it can be inferred that the

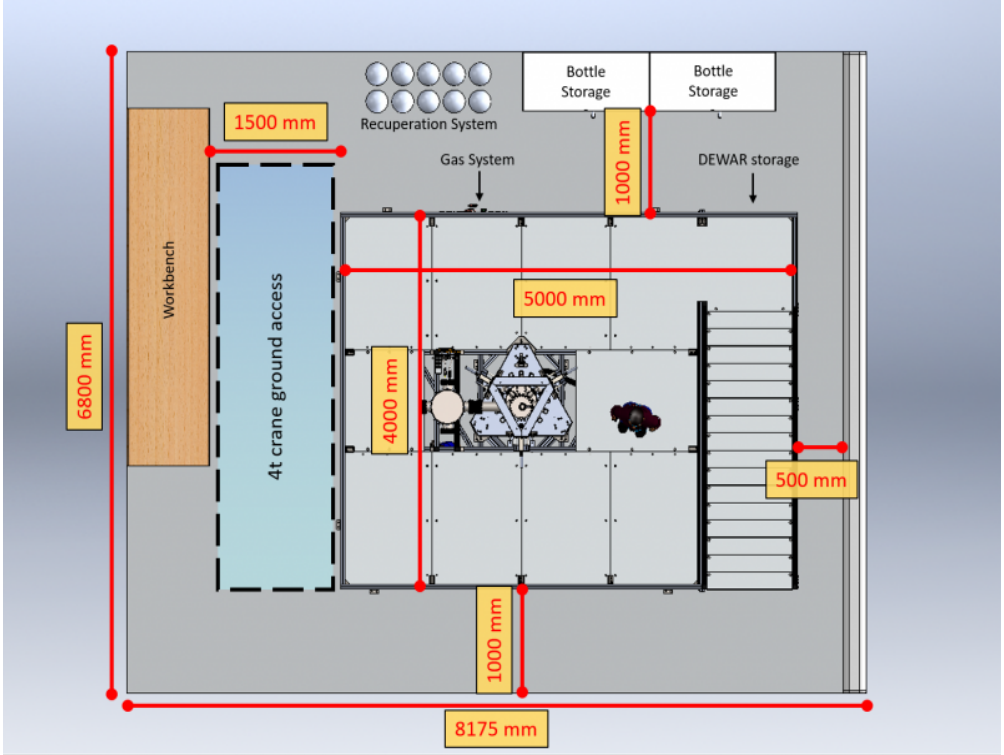

Figure 5.1.: *Layout of the assembly hall where the demonstrator is placed. The outermost boundaries are the concrete walls [51].*

Source	Components	Total mass[kg]	Volume[m^3]
Concrete	walls(after subtracting windows)+roof+floor	21.5×10^4	89.8
Stainless steel	outer+inner cryostat	121.9	1.5×10^{-2}
Copper	140× field shaping rings	8.6	9.6×10^{-4}
PTFE	PMT+SiPM holders, cylinder inside FSR+pillars	10.2	4.6×10^{-3}
PMT	2 pmts	7.3×10^{-2}	9.06×10^{-5}
SiPM	4×26 sipms(12×12mm^2)	6.1×10^{-3}	40.9×10^{-5}

Table 5.2.: *Components mass and volume distribution*

activities of ^{226}Ra and ^{228}Th are significantly lower than that of their parent nuclei. This difference in the activities can lead to disequilibrium [67] due to the varying initial concentrations of the parent and the daughter chain. Hence the daughter chain is separated from the parent chain and the exposure due to each of them is calculated separately.

5.2. Background rate from the concrete walls

From table 5.1 and 5.2, it is clear that concrete has the highest activity per unit mass when compared to other materials. This could imply that the majority of the material background signals detected by the demonstrator TPC comes from the radioactive contaminants in concrete. In this section, an estimate of the rate

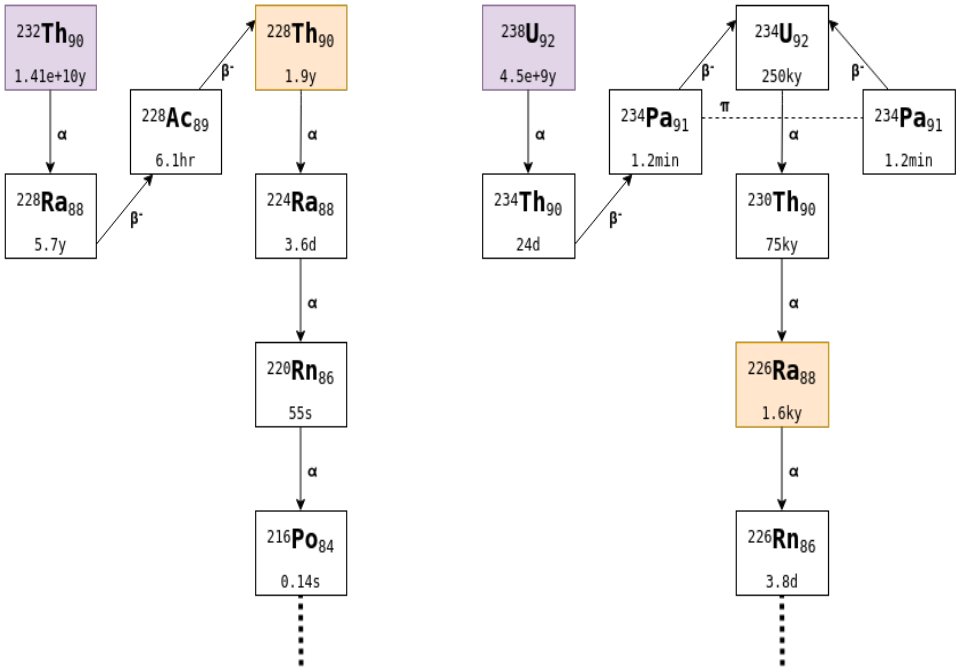

(a) (b)

Figure 5.2.: *a)* ^{232}*Th decay chain b)* ^{238}*U decay chain*

at which the demonstrator records the concrete background is calculated.

Concrete's major radioactive sources are the ^{226}Ra, ^{232}Th and ^{40}K nuclei. The major decay by-products include alphas, beta and gamma radiation. A sheet of paper ($\sim$ 89 μm) absorbs alphas easily. Hence, concrete stops almost all alphas successfully. Similarly betas are significantly stopped too given the high density of concrete ($\sim$ 2400 kg/m^3). Gamma photons manage to escape the concrete volume with a small attenuation given its high penetration power. It is reasonable to assume that the entire background signal contribution from concrete arises from gamma interactions.

Gamma photons are linearly attenuated as a result of Compton scattering with the electrons present in concrete. This can be determined using the following expression [68] :

$$\frac{I}{I_0} = \exp(-\mu x) \tag{5.1}$$

Where μ (cm^{-1}) is the linear attenuation coefficient, x (cm) is the thickness of the sample and I_0 is the photon intensity before attenuation.

The mass attenuation coefficient given by μ/ρ (cm^2/g) where ρ is the density of the material for concrete can be experimentally determined and is $\sim$ 0.055 cm^2/g [69]. Given that the density of concrete is 2400 kg m^{-3}, the linear attenuation factor would be $0.055 \times 2.400 = 0.132$ cm^{-1}.

The overall rate of ERs occurring in the TPC due to background from one wall is given by the following expression:

$$R = \int_0^X A \cdot \rho \cdot B \cdot \Omega \cdot \exp(-\mu x) dx \tag{5.2}$$

Where R is the event rate from one concrete wall, A is the average exposed surface area concrete, X is the thickness of the wall, ρ is the density of concrete, B is the average activity of concrete and Ω is the solid angle.

The parameter Ω is dependent on the dimensions of the TPC, given by (assuming a uniform approximation):

$$\Omega = \begin{cases} l_T \cdot d_T / (D_w^2 \cdot 4\pi) & \text{for walls} \\ d_T^2 / (D_w^2 \cdot 16) & \text{for floor and roof} \end{cases} \tag{5.3}$$

Where l_T is the length of the TPC and d_T is the diameter of the TPC holding. D_w is the average distance of the wall from the TPC.

The parameters used in the estimate are given in table 5.3.

Parameter	**Value**
X	0.2 m
μ	13.2 m^{-1}
ρ	2400 kg/m^3
B	800 Bq/kg
l_T	2.6 m
d_T	0.16 m

Table 5.3.: *Parameters used to estimate concrete background event rate.*

	Floor	$Wall_1$	$Wall_2$	$Wall_3$	$Wall_4$	Roof
A [m^2]	55	48	57	21	25	55
D_w [m]	0.5	4	3.4	4	3.4	6.5
R [Hz]	47546.32	13414.64	22048.24	5868.88	9670.32	281.36
		Total	**rate** =	98829.76	Hz	

Table 5.4.: *Area, average distance and the rate calculated from equation(5.2) for each concrete surface are listed. Total rate is the sum rates from each surface. $Wall_3$ and $Wall_4$ have smaller areas due to the presence of windows.*

The placement of the demonstrator in the assembly hall is depicted in figure 5.1. The concrete hall dimensions are obtained from this plan. Inserting the parameters and integrating equation (5.2), rates for each concrete surface is obtained as listed

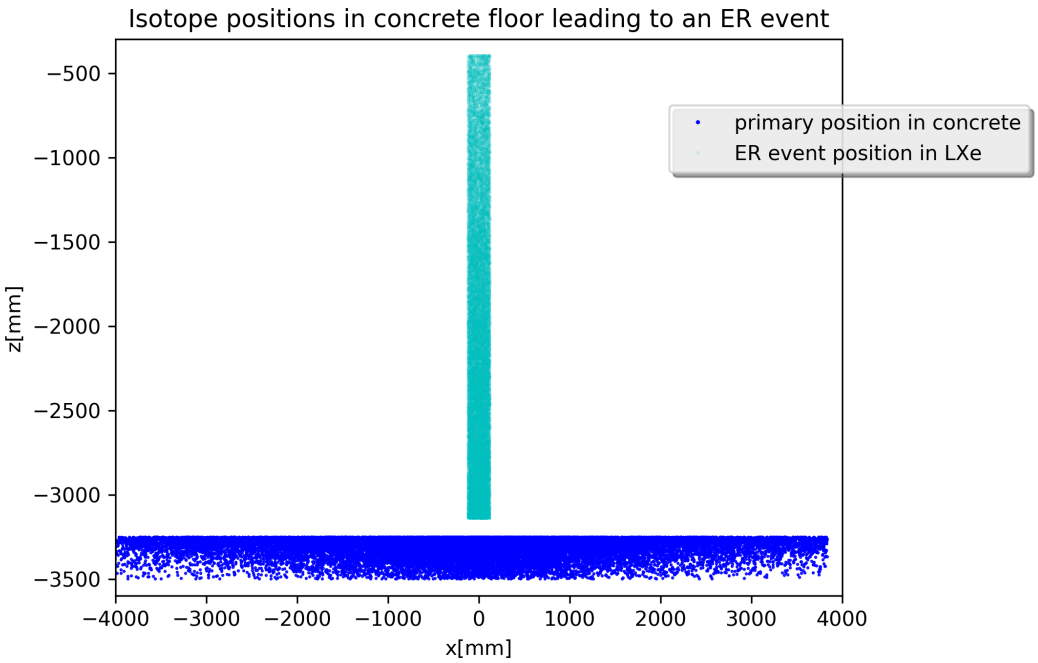

Figure 5.3.: *The blue points represent initial positions of radio-isotopes present in the concrete floor which eventually lead to an ER in LXe (shown in cyan). Note that the radioisotopes were homogeneously distributed in the concrete and attenuation effects played a role in the inhomogeneous distribution of the points that lead to an ER.*

in table 5.4. The rates obtained will be compared with the simulation results, detailed in the following sections. Figure 5.3 shows the simulated points in concrete floor that resulted in ER events in the TPC.

5.3. Simulation Procedure

Monte Carlo simulations using GEANT4 were employed to simulate the background events and its effect on the LXe active volume in the TPC.

The geometry of the TPC as defined in chapter 3 was expanded by including the concrete structure of the assembly hall. Windows of height 4 m were carved out of two walls and the demonstrator was suitably placed on the floor of the assembly hall.

Table 5.2 lists the masses and volume occupied by different materials. After concrete, stainless steel has the larger mass content when compared to other parts of the demonstrator. Hence, the limits to the background calculations can be approximated to be entirely from concrete and stainless steel.

The simulation procedure was executed in the following list of steps:

1. The primary source of interaction i.e., the beginning isotope of the chain

reaction was confined to concrete material and 10^9 events were simulated for concrete.

2. The energy deposition within LXe active volume as a result of interaction with decay products were registered and data was stored in the form of root files.

3. Steps 1 and 2 were repeated by confining the source to stainless steel material in the cryostat.

4. Clustering algorithm was used on the simulation output in order to classify the recorded events into clusters to match the spatial resolution of the detector.

5. The ^{238}U and ^{232}Th chains were split into their daughter chains ^{226}Ra and ^{228}Th respectively.

6. Events collected only in the active LXe volume inside the TPC were separated from the overall events occurring in the total LXe volume.

Once the simulations were completed and the results were processed, the number of events recorded must be scaled in order to obtain a physical interpretation. This scaling requires the knowledge of exposure equivalent in days for each material. In table 5.6, the exposure equivalent in days is listed for concrete and stainless steel. This is calculated using the following formula:

$$T_{eq} = \frac{\text{Number of events}}{W \cdot B_R \cdot Mass \cdot Activity \cdot 3600 \cdot 24} \tag{5.4}$$

Where T_{eq} is the exposure equivalent in years, W is the weight factor and B_R is the branching ratio. Definitions of each are as follows:

Weight factor: The weight factor is a requirement manifested as a result of the working of GEANT4 code. When the number of events to be simulated is mentioned to be 10^9, GEANT4 records each decay process as 1 event. Hence instead of expecting the parent nuclei decaying 10^9 time, it will be divided by the number of daughter nuclei in the chain. This manifestation is corrected for by dividing the exposure equivalent by the *weight factor*. Table 5.5 lists the weight factors for different isotopes.

Branching ratio: The ratio of particles which decay by a single-decay mode to the total number of particles decaying is called branching ratio. The branching ratios of the radioisotopes considered in the current simulations are taken to be approximately equal to 1.

5.4. Electronic Recoil Spectra Results

The ER spectra simulation results for stainless steel and concrete are shown in figures 5.4a and 5.4b respectively in the form of histograms of events occurring

Isotope	Weight factor
^{238}U	14.04
^{226}Ra	14.04
^{232}Th	10.0
^{228}Th	10.0
^{40}K	1.0
^{60}Co	1.0
^{137}Cs	1.95

Table 5.5.: *List of weight factors for different isotopes*

Source	^{238}U	^{226}Ra	$^{228}Ra(^{232}Th)$	^{228}Th	^{40}K	^{60}Co	^{137}Cs
Concrete	-	7.05×10^{-5}	1.02×10^{-4}	-	5.7×10^{-5}	-	-
Stainless steel	32.49	1.69×10^{3}	1.06×10^{3}	1.27×10^{3}	1.53×10^{4}	8.36×10^{2}	3.24×10^{5}

Table 5.6.: *Exposure equivalent in days is listed for concrete and stainless steel.* 10^9 *events were simulated for each radioisotope in each material. The exposure equivalent for concrete is very low (*$\sim 10^{-5}$*) due its high mass content (*$\sim 10^4$ *kg) and large activities (*$\sim 10^2$ *Bq/kg).*

per kg of LXe per day per keV as a function of energy deposited.

The histograms are integrated starting from a particular energy and summed over all the isotopes simulated. Figures 5.5a and 5.5b shows the rate of events occurring as a function of the starting energy from which the integral is calculated.

In case of concrete, the integral from 0 keV to 6000 keV gives the overall rate to be 12079 Hz. This implies that ERs are produced by ^{226}Ra, ^{40}K and ^{232}Th present in concrete at the rate of 12079 events per second. This rate obtained from simulations is approximately an order of magnitude less than the estimate calculated in section 5.2, which was 98830 Hz. This difference arises since the analytic estimate did not take into consideration attenuation of the gamma photons by the cryostat, field shaping rings, LXe itself and other elements of the TPC before it results in an ER event.

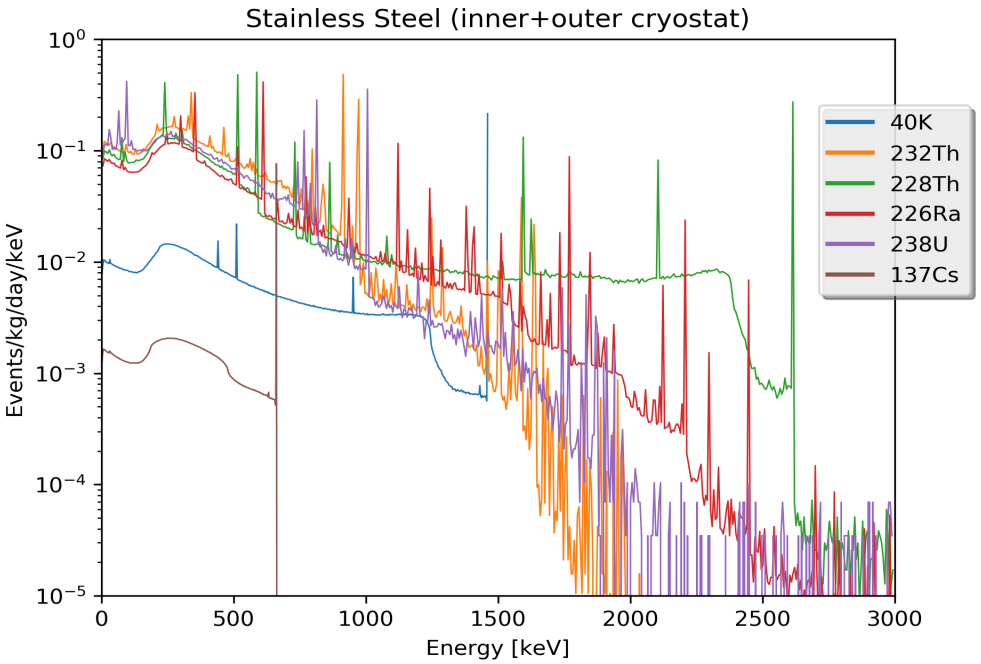

(a)

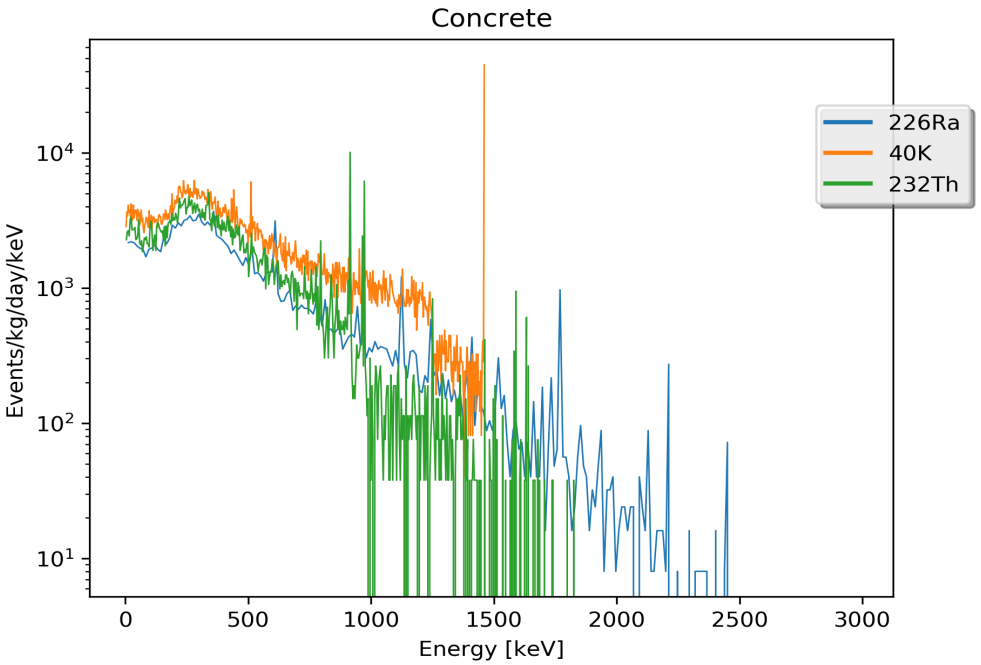

(b)

Figure 5.4.: *Background events from a) stainless steel cryostat b) concrete occurring inside active volume of LXe is plotted as function of energy [keV] of interaction.*

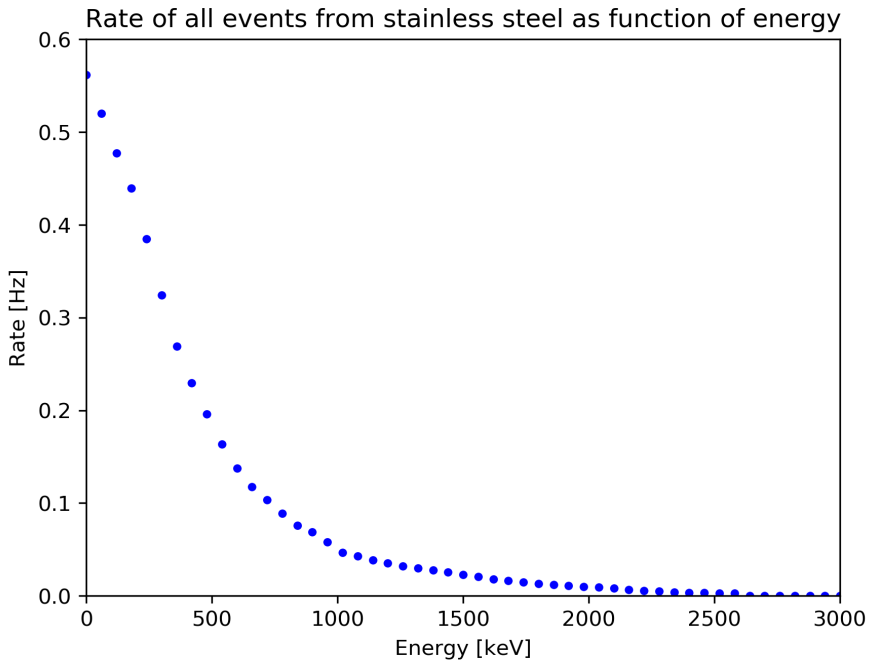

(a)

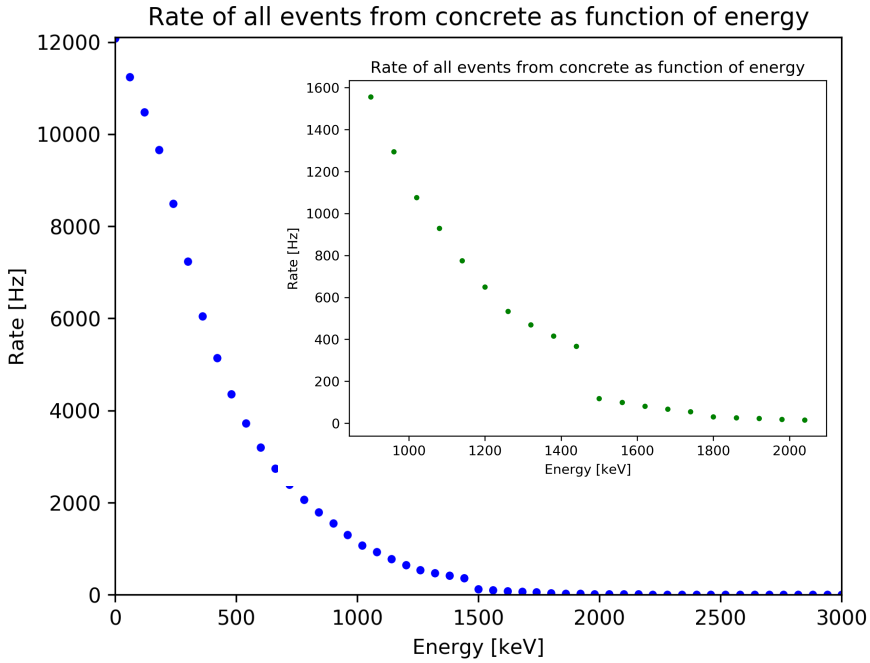

(b)

Figure 5.5.: *The rate of electron recoil events in the LXe active volume as a function of threshold energy from a) stainless steel b) concrete (inset: zoom to lower energies) contaminants. The y-axis is obtained by integrating all the events recorded in LXe starting from the corresponding threshold energies shown on the x-axis*

5.5. Setting the threshold for calibration

This section aims to conclude this thesis work by connecting the simulation results obtained from background studies and light collection efficiency. The goal is to

estimate the number of SiPM rings required for the TPC, so that calibration sources can be suitably separated from background sources.

Based on the length of the demonstrator, the average drift time for the electrons to be accelerated towards the anode is $\sim$ 2 ms [52]. It is not desirable to have background sources interfering with readout within the 2 ms time frame. Figure 5.5b shows that the events rate falls with larger energies. A calibration source is chosen in such a way that its energy is above the energy limit at which the background rate is lower than 100 Hz (corresponding to a 10 ms time frame). In this manner the signal from the calibration source can be separated to a good extent from the background.

The energy above which the background signal frequency is below 100 Hz is set to be the threshold energy. Inferences drawn in the previous sections suggest that the major contributor to the background signals (also to signals around 100 Hz) is concrete. The rates from stainless steel at all energies is less than 1 Hz as can be seen in figure 5.5a and can be considered to as negligible. In case of concrete, the rate of events less than 100 Hz corresponds to energies above 1.6 MeV. Hence, gammas which deposit an energy of 1.6 MeV in LXe sets the threshold.

In order to establish the number of SiPM rings required in the TPC to record events occurring above the threshold, an estimate of the number of photons scintillated per event is required. A simulation package called Nobel Element Simulation Technique (NEST) [70] is used for this purpose. NEST is a simulation package developed at UC Davis. It is mainly built upon experimentally established properties of noble elements. In this regard, it provides sufficiently accurate simulations for scintillation, ionization and electroluminescence processes.

The number of photons generated per event obtained from NEST[1] is scaled by the light collection efficiency of the TPC to obtain the number of photons detected by the photosensors.

5.5.1. Alpha calibration source

A suitable calibration source for the demonstrator experiment would be a radioactive nucleus which, upon decay produces an energetic charged particle ($\sim$ 5 MeV). This particle produces a recoil in the active LXe medium in the TPC such that the number of VUV photons generated exceeds the threshold from the background.

^{220}Ra is a preferred candidate for the calibration source since its decay releases alphas with energies more than 6 MeV [71]. The alpha particles released during this decay process reacts with xenon atoms in the following ways producing electrons and photons:

[1] The calculator available in this website was used: http://nest.physics.ucdavis.edu/download/calculator

$$\alpha + \mathrm{Xe} \rightarrow e + \mathrm{Xe}^{+} + \alpha' \tag{5.5}$$
$$\alpha + \mathrm{Xe} \rightarrow \mathrm{Xe}^{*} + \alpha' \tag{5.6}$$
$$e + \mathrm{Xe}^{+} \rightarrow \mathrm{Xe}^{*} \tag{5.7}$$
$$\mathrm{Xe}^{*} \rightarrow \mathrm{Xe} + h\nu \tag{5.8}$$

The excited xenon (Xe^{*}) eventually comes back to its ground state by emitting VUV light [45].

An alpha particle with energy 5 MeV yields 353735 photons upon scattering with LXe as per the NEST calculator results. On the other hand, background gamma photons with a threshold energy of 1.6 MeV yields 53635 photons. In the next section, these photon numbers are combined with light collection efficiency results and a consensus on the number of SiPM rings required is reached.

5.6. Number of SiPM rings required

The function of SiPM rings is to collect photons, which otherwise would not be detected as a relevant signal. The placement of SiPM rings must be such that signals from the calibration source can be detected and significantly distinguished from any background sources. In case of the 2.6 m tall TPC, SiPM rings aims to provide it with the capability of triggering a 5 MeV alpha interaction at any point of the 2.6 m length of the demonstrator. Hence placement of SiPM rings has to be in such a way that at any point of 2.6 m length, the amount of light detected by SiPMs is larger than the threshold from background. The goal is to minimize the number of SiPMs that can achieve the aforementioned task.

In this regard, light collection efficiency of a single ring consisting of one 6×6 mm^2 SiPM is considered. The number of photons detected by this ring for a 5 MeV alpha particle as a function of length of the TPC is calculated. A Gaussian is fitted onto the simulated data for this ring as shown in 5.6.

Further, the maximum number of photons seen by the SiPM due to a threshold background event is calculated by multiplying the total photons produced from a gamma of 1.6 MeV energy with the maximum value of LCE for that ring. This establishes the threshold above which the SiPM could distinguish the calibration signal from background. Given the width of the fitted Gaussian and the threshold level, four equally spaced rings with one SiPM along the TPC would be comfortably sufficient for the demonstrator to overcome the threshold as illustrated in figure 5.7b. When we consider PMTs and SiPM arrays present at the bottom and top of the TPC respectively, three rings with one SiPM each should be sufficient.

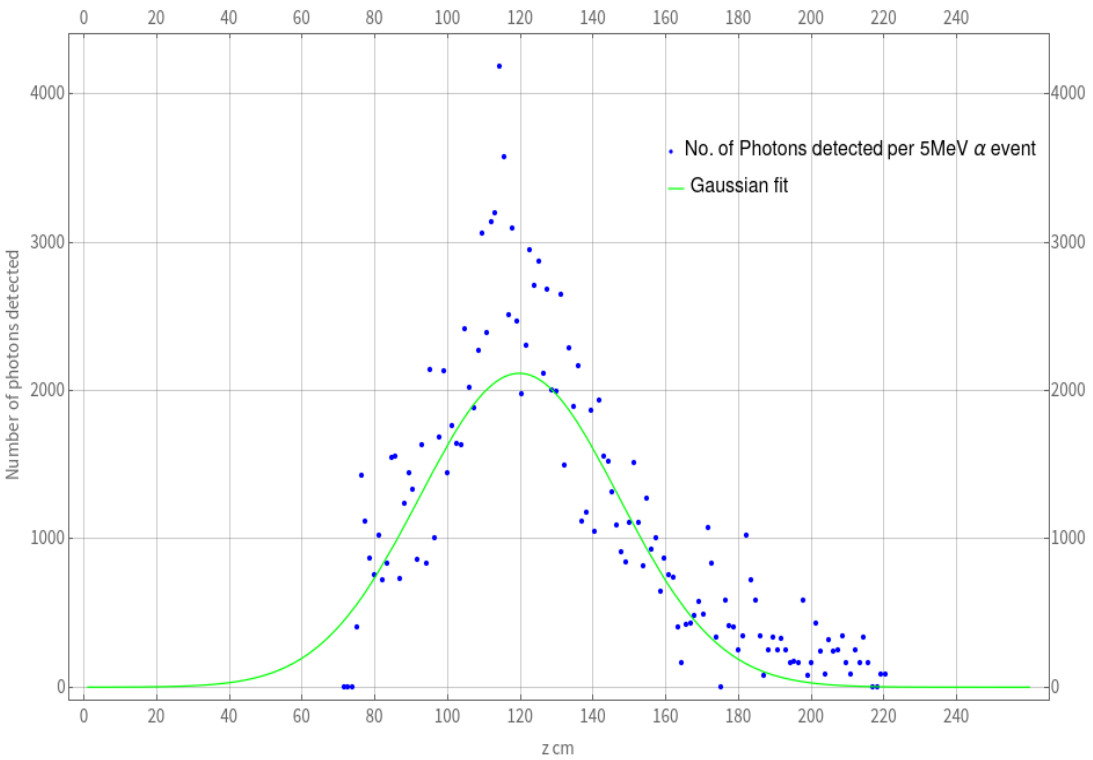

Figure 5.6.: *Fitting the field of view of one SiPM to a Gaussian. Only a part of the data in the 20 cm range about the centre of the SiPM was fit owing to the deviation from Gaussian behaviour after this range as seen in the experiment in chapter 4. In this case, the SiPM ring is placed at z=120 cm.*

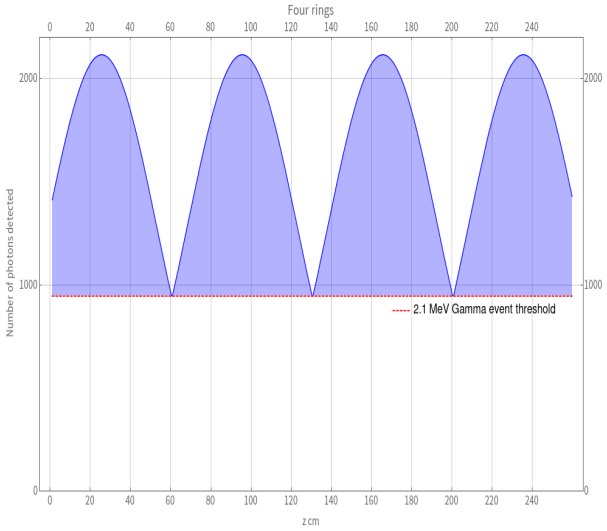

(a)

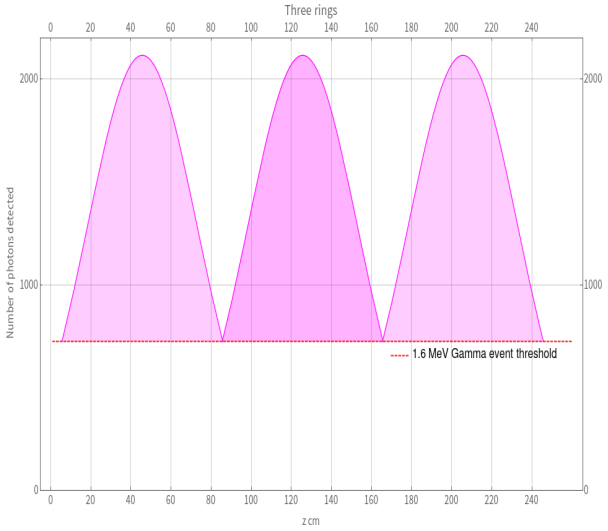

(b)

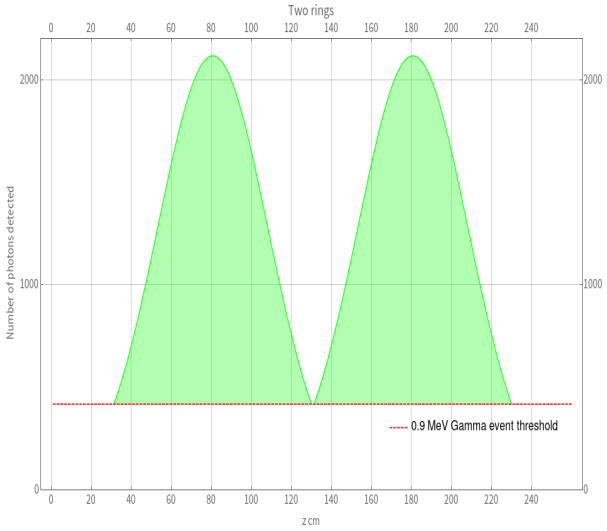

(c)

Figure 5.7.: *A minimum of a) Four rings with one* $6 \times 6\,mm^2$ *SiPM each is required to cover alpha signals of 5 MeV above a threshold of 2.1 MeV over the entire length of the TPC. b) Three rings with one* $6 \times 6\,mm^2$ *SiPM each is required to cover alpha signals of 5 MeV above a threshold of 1.6 MeV over the entire length of the TPC. c) Two rings with one* $6 \times 6\,mm^2$ *SiPM each is required to cover alpha signals of 5 MeV above a threshold of 0.9 MeV over the entire length of the TPC.*

6. Summary

The 2.6 m tall demonstrator as a prototype for DARWIN in the vertical direction, posed design optimization challenges with regard to the placement of photosensors along the cylindrical surface of its TPC. This thesis work was dedicated to studying the TPC photosensor optimization and calibration through simulations and an experiment testing a SiPM field of view.

The first step involved performing light collection efficiency simulations for the TPC with various photosensor placement configurations. The LCE simulation results presented a quantitative estimate of the LCE of the demonstrator TPC as a function of its height for different configurations of SiPM rings.

Further, the experiment performed to test the behaviour of the field of view of a single SiPM in an environment geometrically similar to that of the demonstrator TPC, resulted in the knowledge of the behaviour of the field of the view of SiPM in a real scenario. The experiment was performed for three different configurations of the SiPM. The results show that it is best to have the SiPM closest to the PTFE surface in the TPC to maximize the field of view.

The next part of the thesis which involved simulating ER spectrum from extrinsic radiogenic background helped establish a threshold energy above which calibration events can be distinguishable from background signals. This threshold value jointly with LCE results established an optimized requirement for the number of SiPM rings. A minimum of three SiPM rings containing one 6×6 mm^2 SiPM unit each is sufficient to identify events occurring due to a 5 MeV alpha calibration source across the total length of the TPC.

The radiogenic activity in concrete was taken to be 800 Bq/kg. While this value is an assumption, the activities in concrete could be different at the demonstrator assembly hall. Actual measurements of the gamma flux from concrete is needed to be performed in the demonstrator assembly hall in order to establish an accurate threshold for the calibration of the demonstrator TPC.

List of Figures

List of Tables

Bibliography

[1] F. Zwicky. Die Rotverschiebung von extragalaktischen Nebeln. *Helvetica Physica Acta*, 6:110–127, 1933.

[2] F. Zwicky. On the Masses of Nebulae and of Clusters of Nebulae. , 86:217, October 1937.

[3] V. C. Rubin and W. K. Ford, Jr. Rotation of the Andromeda Nebula from a Spectroscopic Survey of Emission Regions. *APJ*, 159:379, February 1970.

[4] K. G. Begeman, A. H. Broeils, and R. H. Sanders. Extended rotation curves of spiral galaxies: dark haloes and modified dynamics. *Monthly Notices of the Royal Astronomical Society*, 249(3):523–537, 04 1991.

[5] M. Milgrom. A modification of the Newtonian dynamics as a possible alternative to the hidden mass hypothesis. *APJ*, 270:365–370, July 1983.

[6] A. A. Penzias and R. W. Wilson. A Measurement of Excess Antenna Temperature at 4080 Mc/s. , 142:419–421, July 1965.

[7] C. L. Bennett, A. J. Banday, K. M. Gorski, G. Hinshaw, P. Jackson, P. Keegstra, A. Kogut, G. F. Smoot, D. T. Wilkinson, and E. L. Wright. Four-Year COBE DMR Cosmic Microwave Background Observations: Maps and Basic Results. , 464:L1, June 1996.

[8] N. Jarosik, C. L. Bennett, J. Dunkley, B. Gold, M. R. Greason, M. Halpern, R. S. Hill, G. Hinshaw, A. Kogut, E. Komatsu, D. Larson, M. Limon, S. S. Meyer, M. R. Nolta, N. Odegard, L. Page, K. M. Smith, D. N. Spergel, G. S. Tucker, J. L. Weiland , E. Wollack, and E. L. Wright. Seven-year Wilkinson Microwave Anisotropy Probe (WMAP) Observations: Sky Maps, Systematic Errors, and Basic Results. , 192(2):14, February 2011.

[9] Planck Collaboration. Planck 2015 results - i. overview of products and scientific results. *A&A*, 594:A1, 2016.

[10] UC Berkeley Cosmology Group Jeff Filippini. The cosmic microwave background. http://cosmology.berkeley.edu/Education/CosmologyEssays/The_Cosmic_Microwave_Background.html, 2005.

[11] Davi C. Rodrigues, Valerio Marra, Antonino del Popolo, and Zahra Davari. Absence of a fundamental acceleration scale in galaxies. *Nature Astronomy*, 2(8):668â672, Jun 2018.

[12] J. Lehár, E. E. Falco, C. S. Kochanek, B. A. McLeod, J. A. Muñoz, C. D. Impey, H. W. Rix, C. R. Keeton, and C. Y. Peng. Hubble Space Telescope Observations of 10 Two-Image Gravitational Lenses. , 536(2):584–605, June 2000.

[13] (Johns Hopkins University). Credit: Nasa, esa, m. j. jee and h. ford.

[14] M. Markevitch et al. The bullet cluster. http://chandra.harvard.edu/photo/2006/1e0657/, 2003.

[15] Mariangela Lisanti. Lectures on dark matter physics. *New Frontiers in Fields and Strings*, Nov 2016.

[16] Hitoshi Murayama. Physics beyond the standard model and dark matter, 2007.

[17] C. Alcock et al. The MACHO project: Microlensing results from 5.7 years of LMC observations. *Astrophys. J.*, 542:281–307, 2000.

[18] Steven Weinberg. A new light boson? *Phys. Rev. Lett.*, 40:223–226, Jan 1978.

[19] Daniel J. H. Chung, Edward W. Kolb, and Antonio Riotto. Superheavy dark matter. *Physical Review D*, 59(2), Nov 1998.

[20] Alexander Kusenko. Sterile neutrinos: The dark side of the light fermions. *Physics Reports*, 481(1-2):1â28, Sep 2009.

[21] M. Ackermann et al. Search for gamma-ray spectral lines with the fermi large area telescope and dark matter implications. *Phys. Rev. D*, 88:082002, Oct 2013.

[22] M. L. Ahnen et al. Indirect dark matter searches in the dwarf satellite galaxy Ursa Major II with the MAGIC Telescopes. *JCAP*, 1803(03):009, 2018.

[23] H.E.S.S. Collaboration. Search for a dark matter annihilation signal from the galactic center halo with h.e.s.s. *Phys. Rev. Lett.*, 106:161301, Apr 2011.

[24] M. G. Aartsen et al. Search for annihilating dark matter in the Sun with 3 years of IceCube data. *Eur. Phys. J.*, C77(3):146, 2017. [Erratum: Eur. Phys. J.C79,no.3,214(2019)].

[25] S. AdriÃ¡n-MartÃnez et. al. Limits on dark matter annihilation in the sun using the antares neutrino telescope. *Physics Letters B*, 759:69 – 74, 2016.

[26] Lars Bergström, Torsten Bringmann, Ilias Cholis, Dan Hooper, and Christoph Weniger. New limits on dark matter annihilation from alpha magnetic spectrometer cosmic ray positron data. *Phys. Rev. Lett.*, 111:171101, Oct 2013.

[27] Lyndon Evans and Philip Bryant. LHC machine. *Journal of Instrumentation*,

3(08):S08001–S08001, aug 2008.

[28] R. Bernabei et al. The DAMA/LIBRA apparatus. *Nucl. Instrum. Meth.*, A592:297–315, 2008.

[29] F Froborg and. SABRE: WIMP modulation detection in the northern and southern hemisphere. *Journal of Physics: Conference Series*, 718:042021, may 2016.

[30] Angloher, G. et.al. Results from 730 kgs of the cresst-ii dark matter search. *Eur. Phys. J. C*, 72(4):1971, 2012.

[31] R. Agnese et. al. Projected sensitivity of the supercdms snolab experiment. *Phys. Rev. D*, 95:082002, Apr 2017.

[32] E. Armengaud et.al. Performance of the EDELWEISS-III experiment for direct dark matter searches. *Journal of Instrumentation*, 12(08):P08010–P08010, aug 2017.

[33] A. Aguilar-Arevalo et.al. Search for low-mass wimps in a 0.6 kg day exposure of the damic experiment at snolab. *Phys. Rev. D*, 94:082006, Oct 2016.

[34] C. Amole et.al. Dark matter search results from the PICO$-$60 c_3f_8 bubble chamber. *Phys. Rev. Lett.*, 118:251301, Jun 2017.

[35] K. Abe et al. Light WIMP search in XMASS. *Phys. Lett.*, B719:78–82, 2013.

[36] P. A. Amaudruz et al. Design and Construction of the DEAP-3600 Dark Matter Detector. *Astropart. Phys.*, 108:1–23, 2019.

[37] P. Agnes et al. First Results from the DarkSide-50 Dark Matter Experiment at Laboratori Nazionali del Gran Sasso. *Phys. Lett.*, B743:456–466, 2015.

[38] J. Calvo et al. Commissioning of the ArDM experiment at the Canfranc underground laboratory: first steps towards a tonne-scale liquid argon time projection chamber for Dark Matter searches. *JCAP*, 1703(03):003, 2017.

[39] E. Aprile and et.al. First dark matter search results from the xenon1t experiment. *Phys. Rev. Lett.*, 119:181301, Oct 2017.

[40] D N McKinsey. The LZ dark matter experiment. *Journal of Physics: Conference Series*, 718:042039, may 2016.

[41] XiGuang Cao and et.al. Pandax: a liquid xenon dark matter experiment at cjpl. *Science China Physics, Mechanics & Astronomy*, 57(8):1476–1494, Aug 2014.

[42] J. Aalbers et.al. DARWIN: towards the ultimate dark matter detector. *Journal of Cosmology and Astroparticle Physics*, 2016(11):017–017, Nov 2016.

[43] Marc Schumann. Dark matter search with liquid noble gases, 2012.

[44] Teresa MarrodÃ¡n Undagoitia and Ludwig Rauch. Dark matter direct-detection experiments. *Journal of Physics G: Nuclear and Particle Physics*,

43(1):013001, Dec 2015.

[45] E. Aprile and T. Doke. Liquid xenon detectors for particle physics and astrophysics. *Reviews of Modern Physics*, 82(3):2053â2097, Jul 2010.

[46] U. Asaf and I. T. Steinberger. Photoconductivity and electron transport parameters in liquid and solid xenon. *Phys. Rev. B*, 10:4464–4468, Nov 1974.

[47] A. Baldini, C. Bemporad, F. Cei, T. Doke, M. Grassi, A.A. Grebenuk, D.N. Grigoriev, T. Haruyama, K. Kasami, J. Kikuchi, and et al. Absorption of scintillation light in a 100l liquid xenon -ray detector and expected detector performance. *Nuclear Instruments and Methods in Physics Research Section A: Accelerators, Spectrometers, Detectors and Associated Equipment*, 545(3):753â764, Jun 2005.

[48] Lutz Althuse. Xenon1t plots. xenon1t internal note, 2018.

[49] F. Agostini et.al. Sensitivity of the darwin observatory to the neutrinoless double beta decay of ^{136}xe, 2020.

[50] L. Baudis, A. Ferella, A. Kish, A. Manalaysay, T. Marrodán Undagoitia, and M. Schumann. Neutrino physics with multi-ton scale liquid xenon detectors. *Journal of Cosmology and Astroparticle Physics*, 2014(01):044–044, jan 2014.

[51] Image credits F Girard. Uzh.

[52] Laura Baudis. The search for dark matter. *European Review*, 26(1):70â81, 2018.

[53] Image credits N Mcphadden. Uzh.

[54] S. Agostinelli et.al. Geant4âa simulation toolkit. *Nuclear Instruments and Methods in Physics Research Section A: Accelerators, Spectrometers, Detectors and Associated Equipment*, 506(3):250 – 303, 2003.

[55] Jim Pivarski, Pratyush Das, Chris Burr, Dmitri Smirnov, Matthew Feickert, Tamas Gal, Nicholas Smith, Noah Biederbeck, Oksana Shadura, Mason Proffitt, benkrikler, Hans Dembinski, Henry Schreiner, Jonas Rembser, Marcel R., Chao Gu, Jonas RÃ$\frac{1}{4}$benach, Michele Peresano, and Ruggero Turra. scikit-hep/uproot: 3.11.7, June 2020.

[56] V.N.Solovov et.al. Measurement of the refractive index and attenuation length of liquid xenon for its scintillation light. *Nuclear Instruments and Methods in Physics Research Section A: Accelerators, Spectrometers, Detectors and Associated Equipment*, 516(2-3):462â474, Jan 2004.

[57] Hamamatsu Photonics K.K. What is an sipm and how does it work?

[58] Avalanche photodiodes (apds).

[59] Hamamatsu Photonics. "mppcs (sipms)/mppc arrays".

[60] What is mppc (sipm)?: Multi-pixel photon counters (mppcs/sipms).

[61] L. Baudis, M. Galloway, A. Kish, C. Marentini, and J. Wulf. Characterisation of silicon photomultipliers for liquid xenon detectors. *Journal of Instrumentation*, 13(10):P10022âP10022, Oct 2018.

[62] Aalbers J. Agostini F. et al. Aprile, E. Removing krypton from xenon by cryogenic distillation to the ppq level. *Eur. Phys. J. C*, 77(275), May 2017.

[63] Karin BrodÃ©n et.al. Radioactivity in commercially available metals. *NKS*, 49, Dec 2001.

[64] City of Zurich (Switzerland). A low carbon, circular economy approach to concrete procurement. *GPP In practice*, 88(10), May 2019.

[65] Konstantin Kovler. The national survey of natural radioactivity in concrete produced in israel. *Journal of Environmental Radioactivity*, 168:46 – 53, 2017. Naturally Radioactivity in Construction.

[66] Aalbers J. Agostini F. et al. Aprile, E. Material radioassay and selection for the xenon1t dark matter experiment. *Eur. Phys. J. C*, 77(890), 2017.

[67] XENON100 Collaboration. Study of the electromagnetic background in the xenon100 experiment, 2011.

[68] El-Sayed A. Waly and Mohamed A. Bourham. Comparative study of different concrete composition as gamma-ray shielding materials. *Annals of Nuclear Energy*, 85:306 – 310, 2015.

[69] Shamsan S. Obaid, Dhammajyot K. Gaikwad, and Pravina P. Pawar. Determination of gamma ray shielding parameters of rocks and concrete. *Radiation Physics and Chemistry*, 144:356 – 360, 2018.

[70] M Szydagis, N Barry, K Kazkaz, J Mock, D Stolp, M Sweany, M Tripathi, S Uvarov, N Walsh, and M Woods. Nest: a comprehensive model for scintillation yield in liquid xenon. *Journal of Instrumentation*, 6(10):P10002âP10002, Oct 2011.

[71] Rafael F. Lang, Andrew Brown, Ethan Brown, Mayra Cervantes, Sean Macmullin, Darryl Masson, Jochen Schreiner, and Hardy Simgen. A ^{220}Rn source for the calibration of low-background experiments. *JINST*, 11(04):P04004, 2016.

Appendices

A. Analytic estimate of LCE workings

Here we will see the procedure for calculating the analytic estimation of the light collection efficiency Say, the number of reflections undergone by the photons before it reaches the PMTs is $\leq$ n, the solid angle that reaches the bottom would be:

$$\Omega(h) = \frac{1}{4}(1 - \cos\alpha_1) + \frac{1}{4}(1 - \cos\alpha_2) \tag{A.1}$$

Where,

$$\alpha_1 = \tan^{-1}[\frac{(2n+1)R + r}{h}] \tag{A.2}$$

$$\alpha_2 = \tan^{-1}[\frac{(2n+1)R - r}{h}] \tag{A.3}$$

Integrating this over a disk element at a height h and simplifying the obtained result, we get:

$$f(h) = 1 - \frac{2h}{R^2}[\sqrt{h^2 + 4(2n+1)^2R^2} - h + R\log|\frac{h}{\sqrt{h^2 + 4(2n+1)^2R^2} + 2R}|] \tag{A.4}$$

Taylor expanding the log term to the first order and simplifying, we get:

$$f(h) = 1 - 4h[\frac{(2n+1)^2 - 1}{\sqrt{h^2 + 4(2n+1)^2R^2} + 2(2n+1)R + h}] \tag{A.5}$$

The final expression for light collection efficiency will be (with L_r the Rayleigh scattering length and L_a the absorption length of liquid xenon). The given parameters are listed in the Table(3.2):

$$LCE(h) = (A_{SiPM} \exp[-(H-h) \cdot (\frac{1}{L_r} + \frac{1}{L_a})] f(H-h) \\ + A_{PMT} \exp[-h \cdot (\frac{1}{L_r} + \frac{1}{L_a})] f(h)) \cdot 100 \tag{A.6}$$